ACS APPLIED BIO MATERIALS

www.acsabm.org

Article

Luminescent 11-{Naphthalen-1-yl}dipyrido[3,2-a:2′,3′-c]phenazine-Based Ru(II)/Ir(III)/Re(I) Complexes for HCT-116 Colorectal Cancer Stem Cell Therapy

Utpal Das,[†] Shanooja Shanavas,[†] Apoorva H. Nagendra, Binoy Kar, Nilmadhab Roy, Seshu Vardhan, Suban K Sahoo, Debashis Panda, Bipasha Bose,* and Priyankar Paira*

Cite This: *ACS Appl. Bio Mater.* 2023, 6, 410−424

Read Online

ACCESS | Metrics & More | Article Recommendations | Supporting Information

ABSTRACT: Due to a number of unpleasant considerations, marketed drugs have steadily lost their importance in the treatment of cancer. In order to find a viable cancer cell diagnostic agent, we therefore focused on metal complexes that displayed target adequacy, permeability to cancer cells, high standard water solubility, cytoselectivity, and luminescent behavior. In this aspect, luminescent 11-{naphthalen-1-yl} dipyrido [3,2-a:2′,3′-c] phenazine based Ru(II)/Ir(III)/Re(I) complexes have been prepared for HCT-116 colorectal cancer stem cell therapy. Our study successfully established the possible cytotoxicity of **IrL** complex at different doses on HCT-116 colorectal cancer stem cells (CRCSCs). Additionally, an immunochemistry analysis of the complex **IrL** showed that the molecule was subcellularly localized in the nucleus and other regions of the cytoplasm, where it caused nuclear DNA damage and mitochondrial dysfunction. The level of BAX and Bcl-2 was further quantified by qRT-PCR. The expression of proapoptotic BAX showed increased expression in the complex **IrL**-treated cell compared to the control, indicating the potential of complex **IrL** for apoptotic induction. Upon further validation, complex **IrL** was developed as an inhibitor of autophagy for the eradication of cancer stem cells.

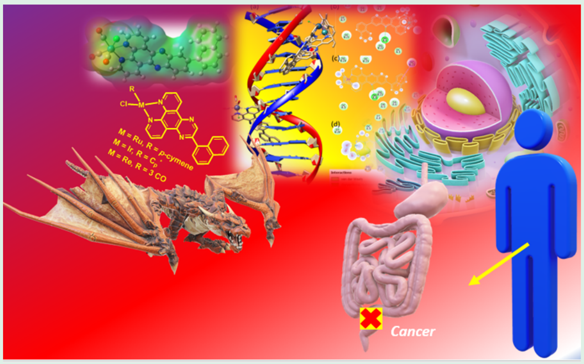

KEYWORDS: *1,10-phenanthroline-5,6-dione, dichloro(p-cymene)ruthenium(II) dimer pentamethylcyclopentadienyliridium(III) chloride dimer, pentacarbonylchlororhenium(I), 11-(naphthalen-1-yl)dipyrido[3,2-a:2′,3′-c]phenazine, DFT analysis, molecular docking, cell cycle analysis*

1. INTRODUCTION

A catastrophic situation in the living world has resulted from the rising menace of cancer, which is now the second most fatal disease in developing nations.[1,2] So, the development of an effective anticancer drug is a challenge for modern scientists. In 1965, Rosenberg discovered cis-diamminedichloroplatinum(II) (cisplatin) and engendered a new path in anticancer research based on metallopharmaceuticals.[3] Cancer treatment has greatly benefited from the extensive applications of platinum drugs.[4] However, due to various harmful effects of this platinum-based drug in normal cells, it′s use has been restricted, prompting researchers to turn to nonplatinum anticancer metallodrugs.[5−8] After being tested on several cancer cell lines, researchers are increasingly interested in ruthenium, iridium, and rhenium-based metallodrugs.[9−20] The activity of ruthenium complex against cisplatin-resistant cells with a minimal toxic response all make delivery to cancer cells simpler and with fewer adverse effects.[21] Some of Ru(II)-arene complexes have previously been reported as water-soluble in nature. High quantum yields, large Stokes shifts, high cellular permeability, a wide range of ligand substitution abilities, low toxicity, long emission lifetimes, potential redox properties, the absorption of two photons, adequate photo stability, and stability toward cancer cell environments are some of the interesting properties of iridium complexes.[22−24] The majority of the reported rhenium compounds were tricarbonyl rhenium complexes, which exhibited rapid and effective cell penetration followed by high cytotoxicity. Some rhenium complexes have recently been designated with their effective photostability and photodynamic therapeutic properties.[25−27] It was also found that complexes containing extensive π-conjugated dipyridophenazine (dppz) as a ligand demonstrate substantial intercalation

Received: June 17, 2022
Accepted: December 28, 2022
Published: January 13, 2023

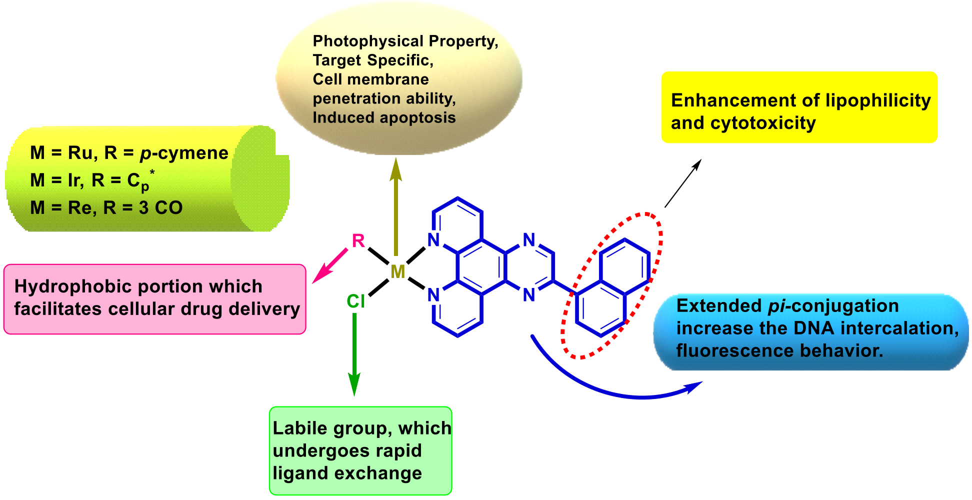

Figure 1. Structural design of 11-{naphthalen-1-yl}dipyrido[3,2-a:2′,3′-c]phenazine-based Ru(II), Ir(III), and Re(I) complexes.

Scheme 1. Synthesis of Ligand (L)

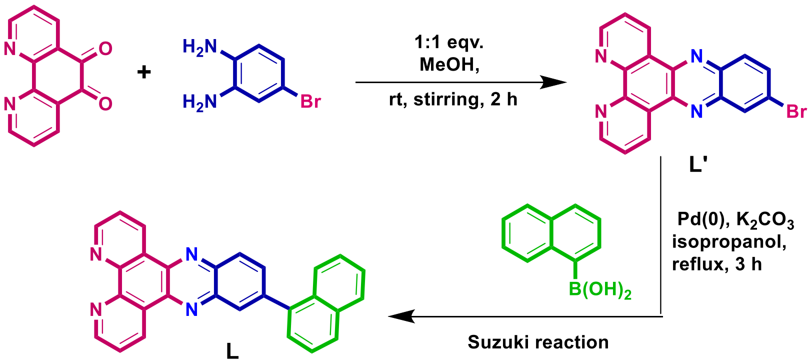

Scheme 2. Synthetic Procedures of Metal Complexes (RuL, IrL, and ReL)

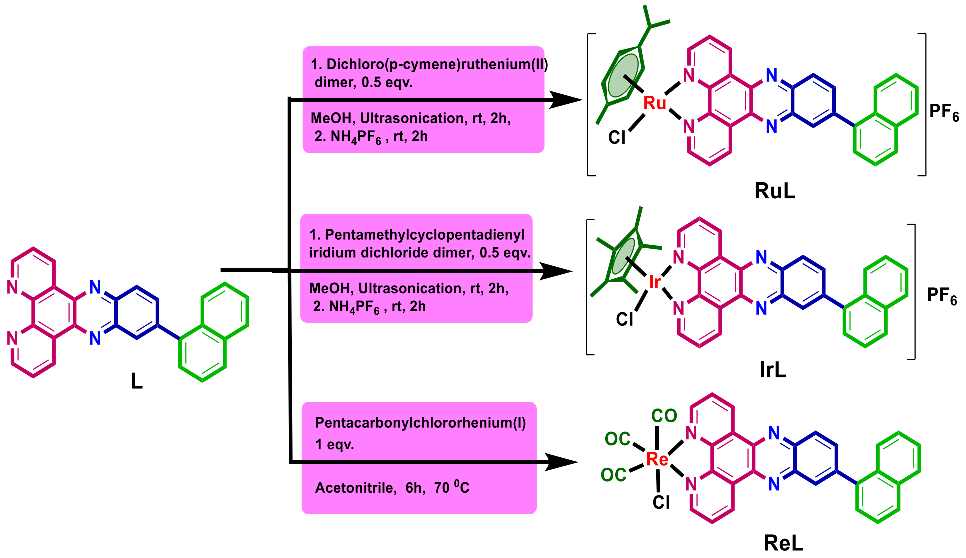

with DNA, reducing steric hindrance between accessory ligands and DNA.[28]

Keeping in mind the advantages of metal and dppz ligand and also encouraged by our previous work with Ir(III)-dppz complex, herein, we have developed dppz-based three metal (Ru/Ir/Re) complexes for selective cancer stem cell therapy (Figure 1).[29] We have also incorporated naphthalene group in the core moiety via Suzuki coupling reaction to enhance the lipophilicity of the complexes and make them more target specific. Potential cellular oxygen sensors have been identified in mitochondria, which have a substantial impact on cellular metabolism.[30] So, the idea of using mitochondria as a primary target for killing cancer cells has been considered. The selective antiproliferative activity of these complexes was evaluated

Table 1. Photophysical Characterization of All Three Complexes RuL, IrL, and ReL

	λ_a (nm)[a]							Λ_M (S m^2 mol^{-1})[g]	
samples	$\pi-\pi^*$	MLCT	λ_f (nm)[b]	O.D.[c]	ε (M^{-1}cm^{-1})[d]	ϕ_f[e]	log $P_{o/w}$[f]	DMSO	10% DMSO
RuL	281	391	467	0.11	3700	0.071	0.33	7	32
IrL	280	387	464	0.20	6700	0.047	0.85	7	49
ReL	273	398	465	0.10	3300	0.055	0.58	6	38
quinine sulfate	350		452	0.25	8000	0.547			

[a] Absorption maxima. [b] Emission wavelength. [c] Optical density. [d] Extinction coefficient. [e] Quantum yield. [f] n-Octanol/water partition coefficient. [g] Conductance in DMSO and 10% aqueous DMSO.

against HCT-116 colorectal cancer stem cells (CRCSCs). The aforementioned complexes showed the ability to destroy cancer cells by inflicting DNA damage, as well as to simultaneously cause mitochondrial disruption through the creation of ROS and control of the Bcl and Bax proteins in our bodies.

2. RESULTS AND DISCUSSION

Chemistry. The design of metal complexes as an innovative anticancer agent required the synthesis of novel ligands. **L′** was synthesized with that goal in mind by reacting one equivalent of 1,10-phenanthroline-5,6-dione with 4-bromo-o-phenylenediamine (1 equiv) in methanol (Scheme 1). The conversion of **L′** to **L** was implemented through Suzuki−Miyaura cross-coupling reaction of **L′** in the presence of Pd (0) as a catalyst and naphthalene-1-boronic acid in isopropanol as depicted in Scheme 1. The characterization of **L′** and **L** was executed by ESI-MS, ^{1}H NMR, ^{13}C NMR, and elemental analysis. The characterized aromatic protons of compound **L′** were observed in the range of 8−10 ppm either as distinct doublets or triplets. Additionally, NMR spectroscopy, ESI-MS, and elemental analyses were used to investigated the ligand (**L**). We found the characteristic 16 protons in the aromatic region of ligand **L** at δ 7−10 ppm. Likewise, characteristic aromatic carbons were observed in the region of δ 124−153 ppm in ^{13}C NMR spectrum. In ESI-MS, the ligand **L**'s distinctive molecular ion peak was seen at 409.233.

Following ligand synthesis, the metal complexes (**RuL**, **IrL**, and **ReL**) was synthesized with 92%−95% yields by reacting the ligand **L** with the respective metal precursors [dichloro(p-cymene) ruthenium(II) dimer, dichloro (pentamethylcyclopentadienyl) iridium(III) dimer, and pentacarbonylchlororhenium(I)] as shown in Scheme 2.

The characterization of all three complexes (**RuL**, **IrL**, and **ReL**) was accomplished by ESI-HRMS, ^{1}H NMR, ^{13}C NMR, ^{19}F NMR, ^{31}P NMR, and elemental analysis. In ^{1}H NMR spectrum, characteristic aromatic peaks of *p*-cymene of complex **RuL** were observed as two distinct doublets in the region of δ 6−7 ppm. In the ^{1}H NMR spectrum, unique peaks of the −Me and −CH protons were visible in the appropriate area. The typical molecular ion peak of **RuL** complex was detected at 679.1212 $[\text{M-PF}_6]^+$ along with ruthenium isotopic splitting. In case of complex **IrL**, the characteristic − Cp* protons were exhibited at 1.755 as singlet. The typical molecular ion peak of **IrL** complex was detected at 771.1861 $[\text{M-PF}_6]^+$. The characteristic −CO peaks of **ReL** complex were identified at δ 182, 190 ppm in ^{13}C NMR. The presence of CO groups in complex **ReL** was further supported by IR spectrum where CO stretching frequency was observed in at 1882 and 2017 cm^{-1}. HRMS, m/z = 720.1027 $[C_{33}H_{19}N_5O_3Re]^+$ (M-Cl $+CH_3CN)^+$, was used to further establish the structure of the complex ReL.

UV−Visible and Fluorescence Study. In 10% dimethylsulfoxide (DMSO), the absorption spectra of all three complexes (**RuL**, **IrL**, and **ReL**) were recorded at 298 K. A strong absorption band ($\pi-\pi^*$) of all the complexes was demonstrated within the bounds of λ 270−280 nm, attributed to spin-allowed intraligand (ligand to ligand) charge transitions (LLCT). Then again, the broad absorption band originating at λ 380−400 nm is due to charge transfer between the metal and the ligand (MLCT) between the respective metal centered HOMO and the molecular orbital of ligand **L** (Figure S1 and Table 1).[31,32] Additionally, it was observed that the MLCT absorption spectrum does not exhibit a red shift, specifying that the inclusion of naphthalene group does not remarkably change the spectral properties, as it is not completely planar with dppz ligand **L′**. To calculate the luminescence quantum yields (ϕ_f) of these complexes, we recorded the emission spectra of all three complexes in 10% DMSO-water (1:9, v/v). Herein, we observed two different emission spectra at 330−340 nm and 460−470 nm after excitation of the complexes at 280 and 395 nm, respectively, and the emission band extended up to 600 nm (Figure S2 and Table 1). The Stoke's shift and luminescence quantum yield values were comparable for all the three complexes at λ_{ex} = 395 nm, and among them, complex **IrL** showed the maximum optical density and Stokes shift but complex **RuL** displayed the highest luminescence quantum yield (ϕ_f) of 0.071 (Table 1).

Assessment of Lipophilicity, Solubility, and Conductivity. To retain the tumor-inhibitory potential of metal complexes, the complex must maintain a balance between hydrophilicity and lipophilicity. The lipophilicity of these complexes has been determined using the conventional shake flask method.[33−35] For metal complexes, the experimental *n*-octanol/water partition coefficient values were acquired in a log $P_{o/w}$ range from 0.33 to 0.85 (Table 1). Among them, complex **IrL** demonstrated the highest log $P_{o/w}$ value of 0.85, which can be attributed to the most hydrophobic nature of the C_p* moiety with iridium metal. The lipophilicity of the complexes are exhibited in the order of **IrL** > **ReL** > **RuL**, which favors the highest cytotoxicity and cellular accumulation of **IrL**. The solubility of all the three metal complexes has been tested in wide range of various solvents. They have shown excellent solubility in dimethyl sulfoxide, acetonitrile, methanol, ethanol, DMF, and fair to good solubility in water. The metal complexes (**RuL**, **IrL**, and **ReL**) exhibited the molar conductance values (Table 1) of ∼32−50 S m^2 mol^{-1} in 10% dimethyl sulfoxide and ∼6−7 S m^2 mol^{-1} in pure dimethyl sulfoxide. The increase in the molar conductivity of these complex in aqueous DMSO can be attributed the dissociation of labile −Cl atom from metal complexes in bulk water media, and proposing their 1:2 and 1:1 electrolytic behavior in 10% dimethyl sulfoxide and pure dimethyl sulfoxide, respectively.[36]

Investigation of Complex Stability by UV−Vis Spectroscopy. To determine whether the three complexes (**RuL**, **IrL**, and **ReL**) are efficient therapeutic agents, their stability was tested in three different medium (1 mM GSH, 10% DMSO-PBS medium, and 10% DMSO-PBS medium in excess NaCl). This is because the complexes must be steady in biological ambience of cells. **RuL**, **IrL**, and **ReL** were revealed to be adequately stable in 1 mM GSH medium up to 48 h as illustrated in Figure S3, indicating that GSH had no such effect on stability of the metal complex. After 48 h, there was a change in absorbance, signifying the slow rate of interaction between GSH and metal complex. A similar tendency was found in 10% DMSO-buffer solution up to 48 h, and when we perform the same experiment in the presence of 110 mM NaCl, no significant changes in absorbance up to 72 h was observed, suggesting that metal complexes are more stable in 10% DMSO-buffer solution with excess NaCl (i.e., under a cellular environment) (Figure S4).

Electrochemical Properties. With the use of cyclic voltammetry and a cleaned gold electrode serving as the working electrode at a set scan rate, the electrochemical activity of the described complexes was investigated to understand the stability of the ruthenium, iridium, and rhenium complexes in (II), (III), and (I) state. The samples were dissolved in 0.1 M of sodium sulfate electrolytic solution at 1 mmol concentration in a 10 mL glass container at a scan rate, 50 mV s^{-1} (Figure 2). Table S1 has all the specific details for the E_o' values of all the complexes. It was discovered that all complexes displayed an irreversible electrochemical behavior according to magnitude of cathodic peak (i_{pc}) and anodic (i_{pa}) currents ($i_{pa} \ll i_{pc}$).[37] Based on the obtained electrode potential values, we believed iridium(III)/iridium(II), ruthenium(III)/ruthenium(II), and rhenium(II)/rhenium(I) were the redox states potential of our synthesized complex. The electroactive performance of produced complexes in water medium was accurately reflected by this discovery.

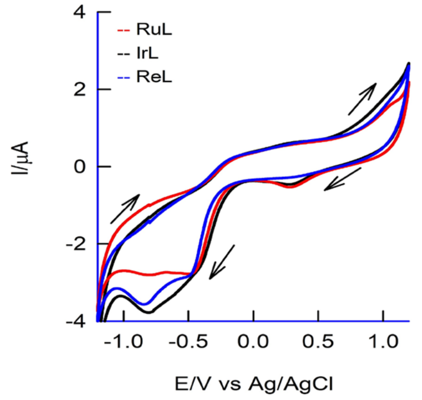

Figure 2. CV report of the synthesized complexes at the potential window of (−1.2 to 1.2) V vs Ag/AgCl in 0.1 M Na_2SO_4 solution at a 50 mVs^{-1} rate of scan.

■ THEORETICAL STUDY

Density Functional Theory. The computational program Gaussian 09W was used to obtain the 3D structure of the complexes (**RuL**, **IrL**, **ReL**), and their different electronic properties.[38] The method based on density functional theory (DFT) was adopted, and the structures were optimized in gaseous phase by spread on B3LYP exchange-correlation energy functional and the basis set LANL2DZ aimed at metal atoms while 6-31G** for the hydrogen, oxygen, carbon, nitrogen, and chlorine atoms. The refined structure and crucial bond lengths are depicted in Figure 3. The computed structure parameters of complex **RuL** and complex **IrL** are found to be identical and formed a pseudo-octahedral geometry. The Ru and Ir center of complex **RuL** and **IrL** resembled the conventional "three leg piano-stool" like structure, in which, η^5-/η^6-arene in the Ru and Ir center of complex **RuL** and **IrL** serves as the stool's seat whereas two coordinated bonds to the nitrogen atoms of naphthyl substituted dppz ligand (**L**) and the bond to chloride atom formed the three legs of the stool. In complex **RuL**, the observed bond angles of N−Ru−Cl and N−Ru−N are 84.61° and 77.81°, respectively, and observed distance from 6 carbons of *p*-cymene ring to the Ru atom are detected between 2.340 to 2.274 Å with average length of 2.299 Å. In **IrL**, observed bond angles for N−Ir−Cl and N−Ir−N are 84.44° and 76.99°, respectively, and observed distance from Ir to five carbon atoms of C_p* are detected between 2.245 to 2.207 Å with average length of 2.226 Å. The Re atom in complex **ReL** is near to perfect octahedral shape, where Re−N, Re−Cl bond distance are slightly larger than the complexes **RuL** and **IrL**.

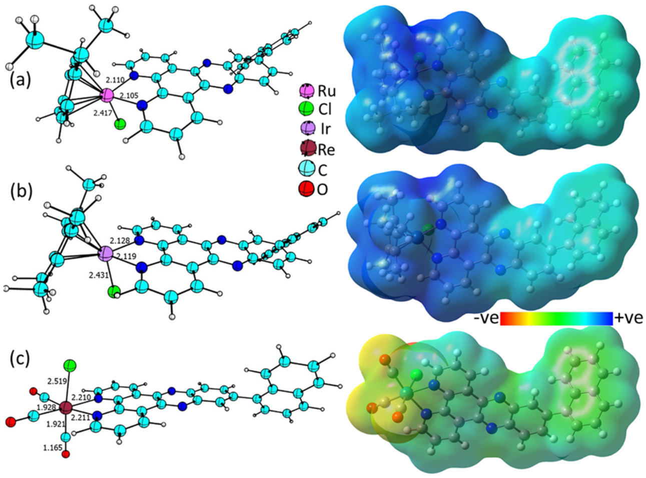

Figure 3. DFT calculated **3D** structure of complexes (a) **RuL**, (b) **IrL**, and (c) **ReL** and their molecular electrostatic map.

Having a different metals center with a highly conjugated dppz ligand (**L**) possessing a twisted naphthalene unit indicating the possible internal charge transfer may occurring in the complexes. Therefore, the DFT computed molecular electrostatic map (MEP) and the HOMO and LUMO diagrams of all these complexes are examines. The MEP showed the negative and positive region in the complexes, where the positive regions are shown in blue color and the red region showed the most negative (Figure 4). In complexes **RuL** and **IrL**, the positive regions dominated around the Ru and Ir center, whereas the most negative part over the naphthalene unit. In contrast, the most negative regions in the complex **ReL** are observed around the Re center. It is expected that in complex **RuL** and **IrL**, the charge transfer is occurred from the naphthalene unit (i.e., from the ligand) to the complex center whereas the reverse process is occurred in the complex **ReL**. To further complement the charge transfer in

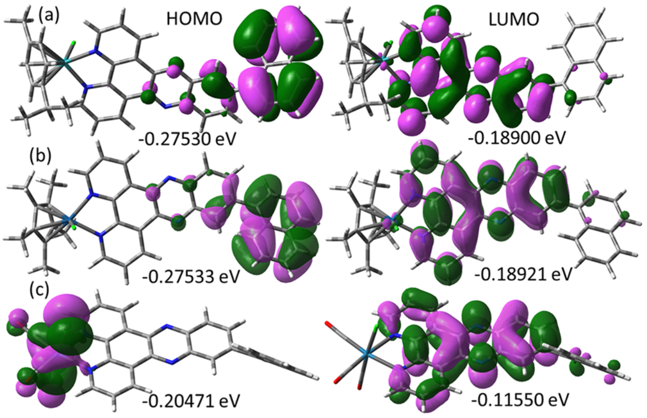

Figure 4. DFT calculated HOMO and LUMO diagrams of complexes (a) **RuL**, (b) **IrL**, and (c) **ReL**.

these complexes, the HOMO and LUMO diagrams are plotted and shown in Figure 4. The HOMO electron density in complexes **RuL** and **IrL** is observed mainly over the naphthalene unit, whereas the LUMO electron density over the phenanthroline and metals (Ru and Ir) center. In contrast, the HOMO electron density is located mainly over the Re center, whereas the LUMO density is mainly over the phenanthroline. These computed results revealed that complexes **RuL** and **IrL** show a similar charge transfer phenomenon but different from that of complex **ReL**.

Molecular Docking Study with DNA and BSA. The interactions of BSA and DNA with synthesized complexes were examined with the help of molecular docking experiments. Using Autodock 4.2 and the Lamarckian genetic method, all dockings were performed.[39] DNA (PDB ID: 1BNA) and BSA (PDB ID: 4SFS) crystal skeletons were collected from the protein database and optimized using Swissmodel. The docking of these complexes with BSA was carried out by adjusting the grid dimensions of *x*, *y*, and *z* with values of 8.376, 21.661, and 106.639, respectively. Albumin abundantly present in the plasma helps to carry and deliver to the target site. BSA with a 66 200 Da molecular mass has the exclusive polypeptide chain of 583 amino acid units.[40] The BSA holds three major domains represented as I, II, and III, and each of them contains 2 subdomains named as A and B. BSA possess two tryptophan (TRP) residues responsible for the intrinsic fluorescence: TRP-134 is located in domain I over the surface of the albumin whereas the TRP212 is present in the binding pocket of subdomain IIA. The complexes **RuL**, **IrL**, and **ReL** docked with BSA showed dock score of −7.68, −8.05, and −7.75 kcal/mol supporting the formation of stable protein−ligand complexes. The complexes **RuL** and **IrL** bind at hydrophobic cavity formed by domains IA, IB, and IIIA, whereas the complex **ReL** best pose located with the

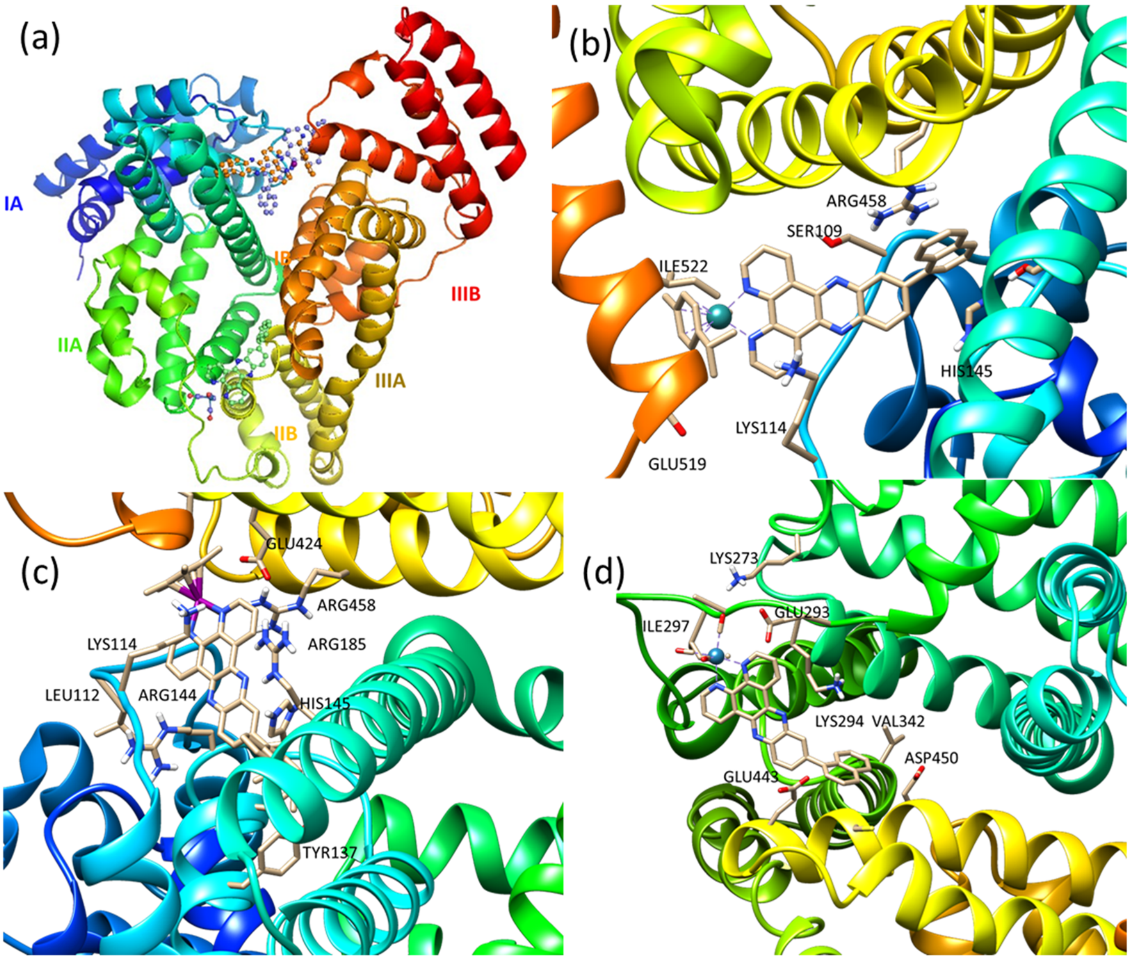

Figure 5. (a) Best pose dock structure of complex **RuL**, complex **IrL**, and complex **ReL** with BSA. The 3D views showing the residues interacting with the complexes in their best pose with BSA: (b) complex **RuL**, (c) complex **IrL**, and (d) complex **ReL**.

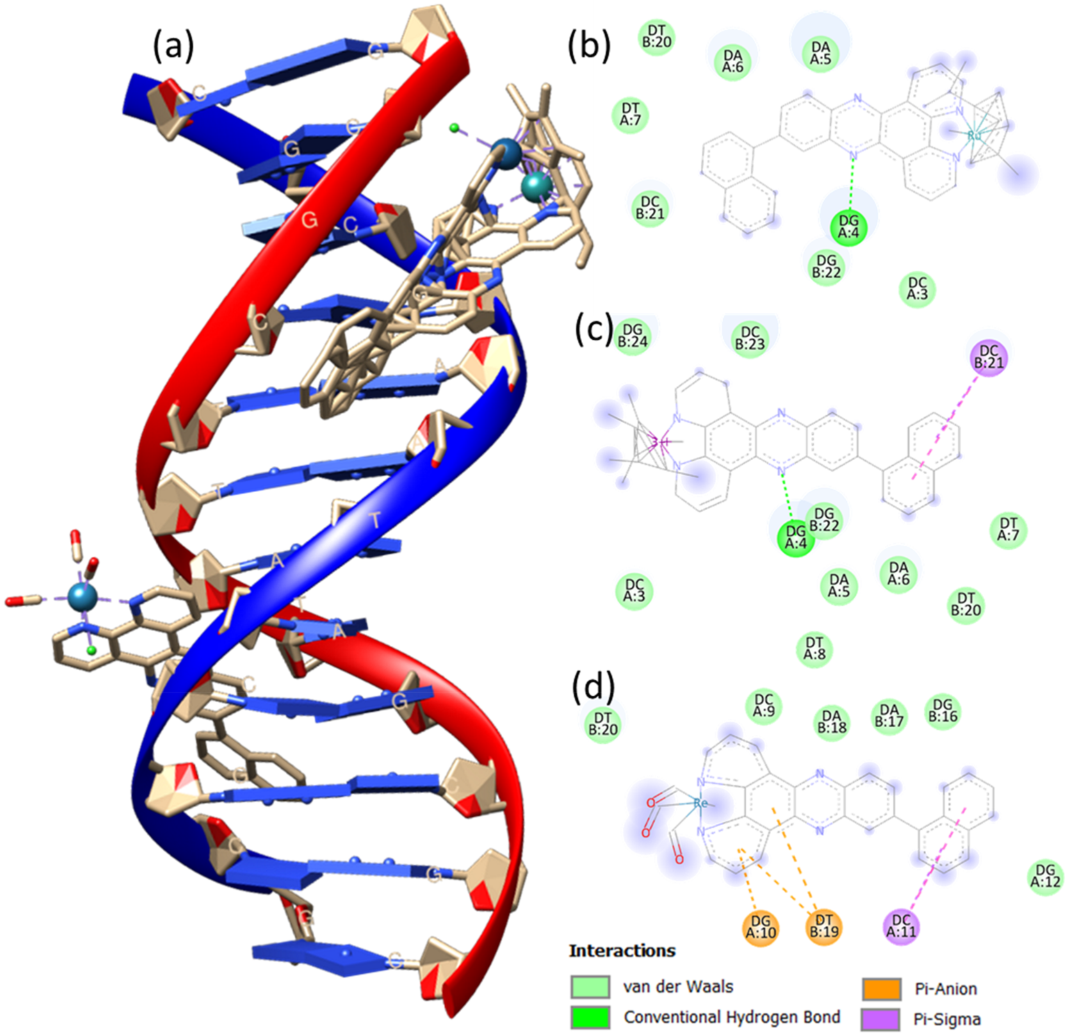

Figure 6. (a) Best dock pose of the complexes with the DNA. 2D structures showing the interactions occurred between the complexes and DNA: (b) complex **RuL**, (c) complex **IrL**, and (d) complex **ReL**.

Table 2. Binding Factors for the Ct-DNA Interaction with All the Complexes

complex	λ_{max} (nm)	change in absorbance intensity	$\Delta\varepsilon$ (%)[a]	k ($\times 10^5$ M^{-1})[a]	K_{SV} ($\times 10^6$ M^{-1})[b]	K_{app} ($\times 10^6$ M^{-1})[c]	n[d]
RuL	284	hypochromism	42	0.083	0.024	2.0	1.74
IrL	282	hypochromism	37	0.082	0.021	2.28	1.49
ReL	295	hypochromism	34	0.093	0.045	2.28	1.32

[a] k, intrinsic DNA binding constant from UV−vis absorption titration. [b] K_{SV}, Stern−Volmer quenching constant. [c] K_{app}, apparent DNA binding constant from competitive displacement. [d] n, number of binding sites.

hydrophobic cavity of IIA, AAB, and IIIA (Figures 5 and 6). The docked structures are stabilized due to the multiple noncovalent interactivities occurred between amino acid residues of BSA and synthesized complexes. Further, the docking experiments of these complexes were performed with DNA by adjusting the grid dimensions of *x*, *y*, and *z* with values of 13.358, 20.325, and 10.766. Complexes **RuL**, **IrL**, and **ReL** have dock scores of −8.60, −8.89, and −10.32 kcal/mol with DNA. Complex **ReL** showed a better dock score with DNA compared to that of complex **RuL** and **IrL**. As shown in Figure 6, the reported complexes are stacked inside of the double helix of DNA. These complexes formed multiple noncovalent interactions with the base pairs of DNA to stabilize the docked structure.

■ DNA BINDING PROPERTY

UV−Visible Study. We performed UV−visible absorption analysis to categorize the different forms of DNA interacting with our **RuL**, **IrL**, and **ReL** complexes. Several compounds can display their potential toward various cancer cells because of their binding ability with DNA. DNA is the crucial pharmacological target for a range of anticancer drugs, and its interaction with metal complexes is a key area for understanding the binding pattern. Electronic transitions are triggered by DNA base pairs called pyrimidine (cytosine and thymine) and purine (adenine and guanine) analogues.[41] Here, we performed a DNA interaction assay for all three complexes using a UV−visible study. The λ_{max} values of complexes **RuL**, **IrL**, and **ReL** were found at 284, 282, and 295 nm, respectively, and they showed hypochromism in absorbance intensity at their respective λ_{max} region with an increase of DNA concentration (Figure S5 and Table 2). The presence of hypochromic shift suggested the intercalative mode of binding between metal complex and DNA. The intrinsic binding constant, (k) values were 0.083×10^5 M^{-1}, 0.082×10^5 M^{-1}, and 0.093×10^5 M^{-1} for **RuL**, **IrL**, and **ReL** complexes respectively (equation ii, Supporting Information, Table 2, Figure S5).

Ethidium Bromide Displacement Assay. Using fluorescence spectroscopy, an ethidium bromide displacement study was performed to confirm the intercalative mode of the binding propensity of **RuL**, **IrL**, and **ReL** complexes with DNA. In this assay, initially, EtBr did not show any kind of fluorescence behavior, but once EtBr was added with Ct-DNA solutions, an intense fluorescence spectrum appeared at λ_{ems} 595 nm upon excitation at λ_{abs} 485 nm owing to the intercalative binding of EtBr with a DNA base pair (Figure S6). Afterthat, every single increment in the concentration of the metal complex developed a hypochromic pattern in fluorescence intensity. It suggests that as the intercalative interaction among DNA and the metal complex progresses, EtBr is displaced from the DNA-EtBr system. By using equation iii (Supporting Information) for **RuL**, **IrL**, and **ReL** complexes, K_{app} (Table 2) were found to be 2.0×10^6 M^{-1}, 2.28×10^6 M^{-1}, and 2.28×10^6 M^{-1}, respectively. The Stern−Volmer quenching constant (K_{SV}) were computed to be 0.024×10^6 M^{-1}, 0.021×10^6 M^{-1}, and 0.045×10^6 M^{-1} by equation iv, (Table 2) for **RuL**, **IrL**, and **ReL** complexes. The important intercalation with Ct-DNA was supported by the considerable hypochromism in absorbance and fluorescence intensity, (K_{app}) and (K) of all metal complexes.

Viscosity Measurement. A viscosity study was accomplished using an Ostwald viscometer to see how the complexes affected the relative specific viscosity of Ct-DNA solutions. Here, we plotted $(\eta/\eta_0)^{1/3}V_S/R$ by using the equation $(\eta/\eta_0)^{1/3} = 1 + \beta R$, where R = [DNA base pairs]/[metal complex], η_0 and η is the specific viscosity of DNA in the absence and presence of the metal complex, and $(\eta/\eta_0)^{1/3}$ = the Ct-DNA solution's relative specific viscosity.[41] A Ct-DNA solution's specific viscosity rose when a metal complex was added to it, following the expected intercalative binding pattern. This is related to base pair separation as well as the accommodation of metal complexes into Ct-DNA base pairs, which increases the length of the Ct-DNA double helix. In the case of partial or nonclassical binding, the binding metal complex may twist the DNA double helix, altering DNA's viscosity and optimum length. Metal complexes engage with the exterior surface of DNA molecules via Van der Waals or hydrophobic interactions in groove binding or electrostatic binding. Here, we looked at the viscosity analysis of all of our synthesized compounds in the presence of Ct-DNA with respect to Ethidium Bromide. The mild increase was found in viscosity of Ct-DNA solution for all the complexes (**RuL**, **IrL**, and **ReL**) upon each addition of metal complex in the Ct-DNA solutions as depicted in Figure S7, describing the intercalative fashion of binding with some extent of electrostatic or groove binding between metal complexes and Ct-DNA.

BSA Binding Property. Serum albumin is a prominent component of plasma proteins that aid in the transport and metabolism of a variety of exogenous and endogenous elements that are involved in cell metabolism. HSA, a structural equivalent of BSA found primarily in cellular environments, aids drug invasion by generating a more active coordinate complex. To investigate the binding ability of metal complexes (**RuL**, **IrL**, and **ReL**) with protein, a BSA binding study was performed using fluorescence titration.[41] In this study, after excitation at 295 nm, the BSA molecule displayed strong fluorescence at 345 nm (Figure S8). The fluorescence intensity of BSA significantly decreased (by more than 50%) when metal complex concentration increased, as can be seen in the plot. With the help of classical Stern−Volmer equation v (Supporting Information), K_q and K_{BSA} were evaluated. For complexes **RuL**, **IrL**, and **ReL**, the K_{BSA} values were found to be 0.0109×10^6 M^{-1}, 0.011×10^6 M^{-1}, and 0.016×10^6 M^{-1}, respectively whereas K_q values were obtained as 1.09×10^{12} M^{-1} S^{-1}, 1.10×10^{12} M^{-1} S^{-1}, and 1.67×10^{12} M^{-1} S^{-1}, respectively (Table 3). Complex **IrL** exhibited the highest binding constant ($K = 2.63 \times 10^4$ M^{-1}) among them. The freshly synthesized complexes had K_q values on the order of 10^{12} M^{-1} S^{-1}, which was greater than the BSA's maximal scatter collision quenching constant value (2.0×10^{10} M^{-1} S^{-1}) and suggested a static quenching linkage. Scatchard equation vi was used (Supporting Information) to compute the binding constants of these complexes as well as the number of binding sites (Table 3). Due to their potent interaction with serum albumin, which overcomes GSH-mediated drug resistance, these complexes have a high level of efficiency in treating cancer cells.[42]

Table 3. Binding Constraints of Complex-BSA Interaction

complex	K_{BSA} ($\times 10^6$ M^{-1})[a]	k_q ($\times 10^{13}$ M^{-1} s^{--1})[b]	K ($\times 10^4$ M^{-1})[c]	n[d]
RuL	0.0109	0.109	1.09	0.98
IrL	0.011	0.110	2.63	1.02
ReL	0.016	0.167	0.94	1.08

[a] K_{BSA}, Stern−Volmer quenching constant. [b] K_q, quenching rate constant. [c] K, binding constant with BSA. [d] n, number of binding sites.

Biology. *Isolation of CD44+ Cancer Stem Cells (CSCs) from HCT-116 Colorectal Cancer Cell Line by Fluorescent Activated Cell Sorting (FACS).* CSCs are the highly resilient subpopulation within a heterogeneous tumor mass incurring the refractoriness toward conventional therapies.[43] The sorting of CD44+ cancer stem cells (CSC) using FACS from the HCT-116 colorectal cancer cell line using antihuman CD44 antibody Alexa flour 488 has resulted in a yield of 92.91% pure population of CSC (Figure 7). The sorted CD44+ CSC population was used for further downstream experiments to explicate the part of synthesized **IrL** complex against the colorectal cancer stem cells.

Cytotoxicity Study of These Complexes on the HCT- 116 CD44+ Cancer Stem Cells. *In vitro* cytotoxicity of **RuL**, **IrL**, and **ReL** complexes along with cisplatin was assessed against HCT-116 derived colorectal cancer stem cells (CRCSCs) via a typical MTT assay. With varying concentrations of these complexes ranging from 1 μM to 500 μM at 37 °C, 5% CO_2, the CRCSCs were incubated for 48 h. Certainly, these complexes were found to be exhibiting dose-dependent cytotoxic effects on the HCT-116 derived CRCSCs. With 4.14 ± 1.2 μM IC_{50} values, complex **IrL** exhibited much higher potency compared to other complexes (IC_{50}: **RuL** = 6.50 ± 1.4 μM and **ReL** = 7.23 ± 1.7 μM) and the positive control cisplatin (IC_{50} ~20 μM) against HCT-116 cell lines tested (Figure 8). Furthermore, validation of the cytotoxic effects mediated by **IrL** complex on HCT-116 was performed with 1

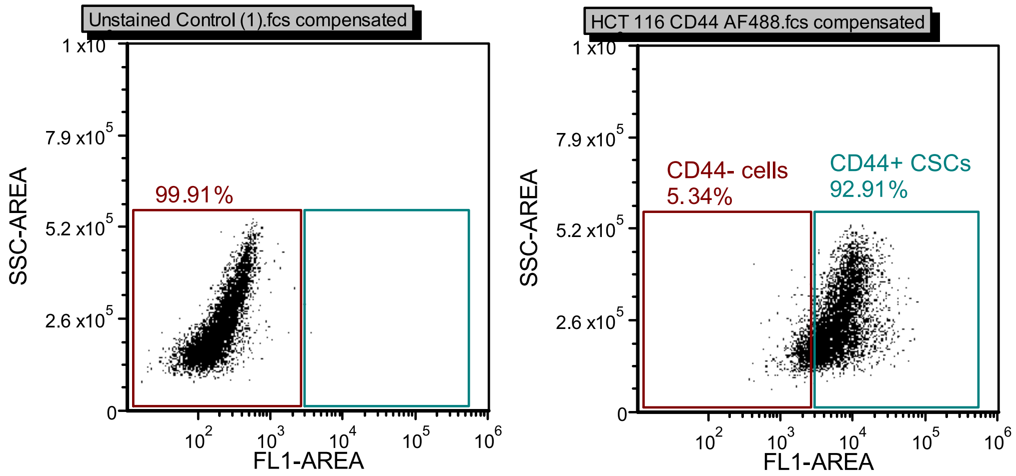

Figure 7. Fluorescent activated cell sorting of cancer stem cells from HCT-116 CSCs

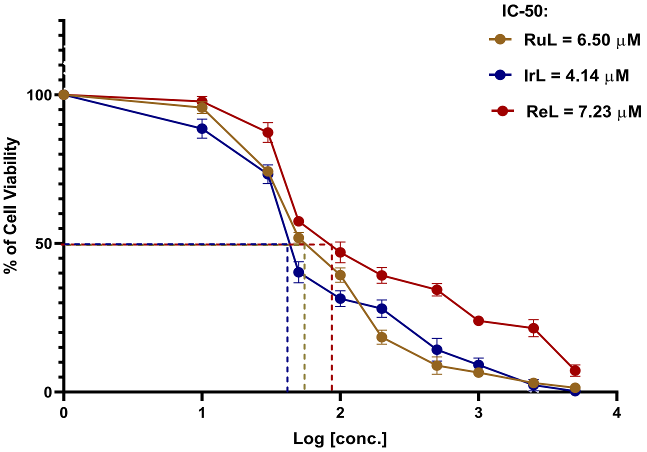

Figure 8. MTT assay for IC_{50} determination of the **RuL**, **IrL**, and **ReL** complex on HCT-116 CD44+ cancer stem cells.

μM, 4 μM, and 8 μM doses on HCT-116 CD44+ cancer stem cells. However, positive control Cisplatin on HCT-116 CD44+ CSCs exhibited much higher IC_{50} (~32 μM) compared to synthesized metal complexes. When all these complexes are subjected to treatment with the normal HEK-293 cell line, the IC_{50} value was greater than 100 (IC_{50} > 100 μM). However, control Cisplatin showed similar efficacy in HEK-293 (IC_{50} ~40 μM) to HCT-116 CD44+ CSCs.

Cellular Localization Study of IrL in HCT-116 Colorectal CSCs. Subcellular localization study of **IrL** in HCT-116 CD44+ CSCs was assessed after treatment of the cells with the aforementioned complex costained with the nuclear dye Hoechst. At concentration of 4 μM, localization in cytoplasm with an emission of red fluorescence was identified by fluorescent imaging of the **IrL**-treated colorectal cancer stem cells (Figure 9). Since the complex has the ability to target mitochondria, an additional experimental validation was done to look at changes in MMP through JC-1 labeling and ROS identification through DCFDA staining.

*Mitochondrial Depolarization/Dysfunction of HCT-116 CSCs by Complex **IrL** in a Dose-Dependent Manner.* To demonstrate the mitochondrial poison and changes in mitochondrial membrane potential (MMP) (ΔΨm), we used CCCP (carbonyl cyanide *m*-chlorophenylhydrazone) treated cells, which mediates dissipation of mitochondrial membrane potential leading to possible mitochondrial dysfunction. Without receiving any therapy, control cells exhibited function like normal mitochondrial, which was measured by flow cytometry. Control cells unveiled ~94% JC-1 aggregates (Red + Green fluorescing healthy mitochondria) and 5.22% JC-1 monomers indicating green fluorescence (Figure 10B). In

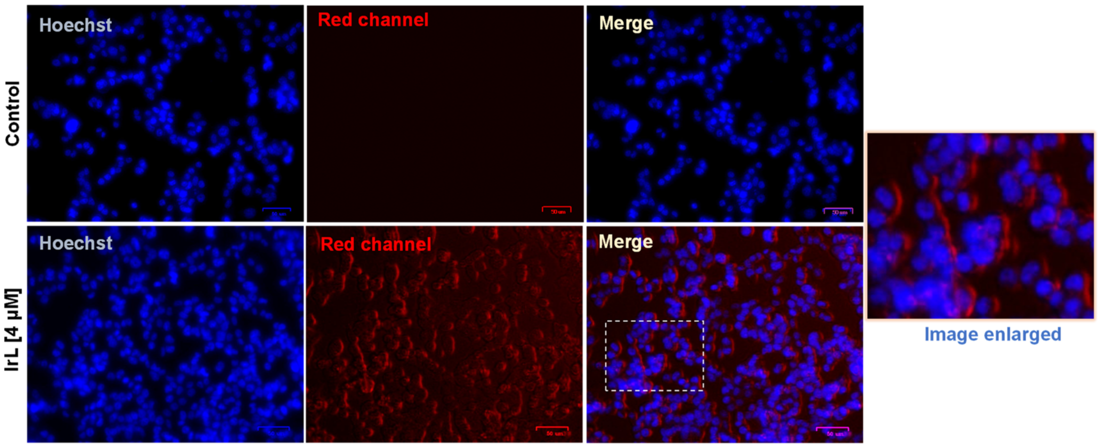

Figure 9. Colocalization assay to demonstrate the Subcellular localization of the **IrL** compound: representative image of the cytoplasmically localized **IrL** complex in HCT-116 CD44+ CSCs, costained with Hoechst. Scale bar 75 μM.

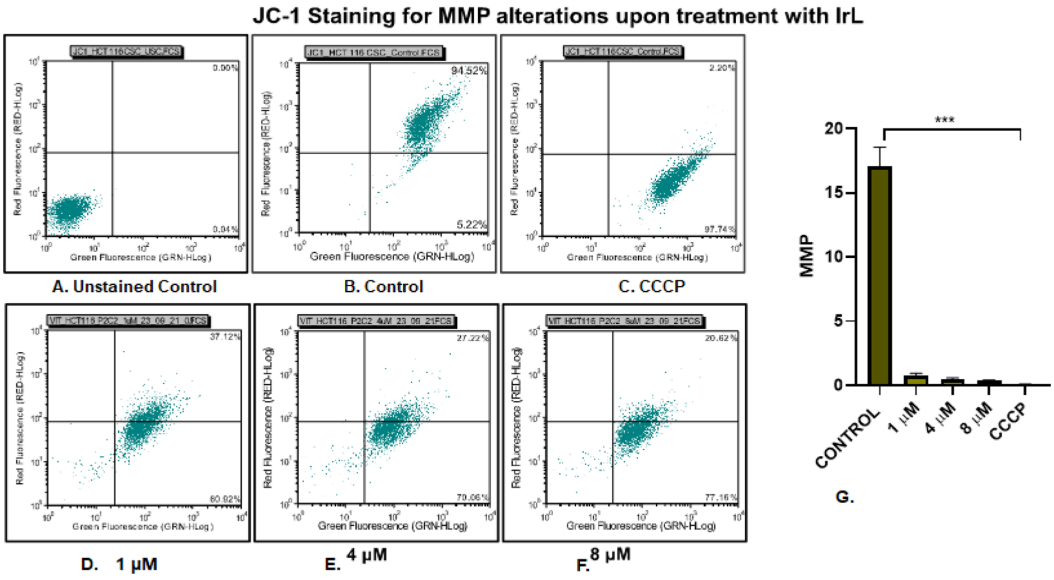

Figure 10. Representative flow cytometric quantification images of JC-1-stained HCT-116 CSCs for the assessment MMP: (A) unstained control for gating purposes, (B) untreated control, (C) positive control (CCCP treated cells), (D) 1 μM treatment, (E) 4 μM treatment, and (F) 8 μM treatment. (G) Graph representing the MMP after **IrL** treatment. The cell with impaired MMP accumulates the monomeric form of the dye and emits green fluorescence. In contrast, the cell population with normal mitochondria emits both red and green fluorescence, comprising an aggregate of both JC monomers and red J aggregates. The observed p value was <0.0001 (***). The error bar represents ± standard error of means (SEM).

contrast to this, the CCCP-treated positive control displayed a high percentage of cells (~97%) with mitochondrial damage (Figure 10C). Green fluorescence was observed in the dose-reliant way in JC-1 monomers (Figure 10D−F) corresponding to spoiled mitochondria in IrL-treated HCT-116 CD44+ CSCs. According to Figure 10D, a 1 μM **IrL** compound concentration contributed to spoiled mitochondria in 60% cells. According to Figure 10E, F, significant changes in MMP and concomitant mitochondrial damage (70% and 77%, respectively) were mediated by increased doses of 3 μM and 5 μM **IrL** complex in HCT-116 CD44+ CSCs. The proportion of green fluorescing JC-1 monomers directly signifies the alteration in the MMP leading to mitochondrial depolarization and associated mitochondrial dysfunction. These results reveal that **IrL** complex mediated cell death (Figure 10C) is dose-reliant when compared to protonophore-CCCP-treated positive control cells. CSCs displaying higher antioxidant activity tends to express higher resistance to ROS induced damage, consequently resulting in lower mitochondrial damage, preserving the mitochondrial membrane potential ($\Delta\Psi_m$).[44]

Immunocytochemistry. Damage to nuclear DNA can also cause mitochondrial dysfunction following the onset of apoptosis. To know this behavior of the complex **IrL**, we performed Gamma H2Ax staining of the cells after complex treatment. Subsequently, we analyzed probable DNA damage in the IrL-treated CSCs by γH2AX staining. The presence of phosphorylated histone mediated by the complex suggests the involvement of the **IrL** complex in arbitrating DNA damage (Figure 11) in CSCs derived from HCT-116. This result concluded that the complex **IrL** localized in nucleus and other part of the cytoplasm and created nuclear DNA damage and mitochondrial dysfunction.

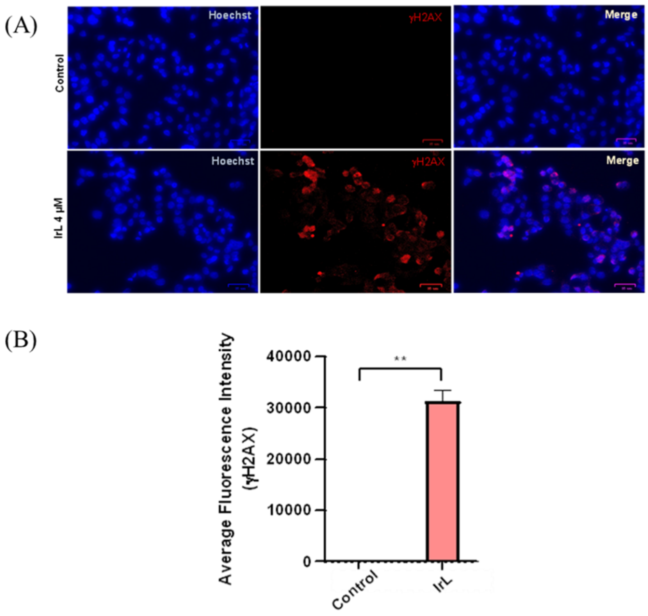

Figure 11. γH2AX staining for the detection of double stranded DNA breaks and subsequent DNA damage: (A) Image representing the expression of γH2AX, indicative of phosphorylated histone associated with DNA damage. Scale bar 35 μm. (B) Graph representing the quantification of red fluorescence intensity concomitant with γH2AX expression.

*ROS Generation through a Dose-Dependent Manner in HCT-116 Cancer Stem Cells by **IrL** Complex Incubation.* The degree of intracellular ROS production is a sign of cellular stress that results in cell death at high ROS levels. By treating HCT-116 CD44+ CSCs with 1 μM and 4 μM concentrations of **IrL**, we were able to show that ROS production increased. The detailed methodology was adapted from Bose et al.[45] When DCFDA is deacetylated and oxidized by reactive oxygen species (ROS) and cellular esterases, the resulting DCF is a green fluorescing compound. The average DCF fluorescence increased in a dose-dependent manner from a 1 μM to 4 μM concentration of the aforementioned complex. ROS production is found to be negligible in the untreated control. On the

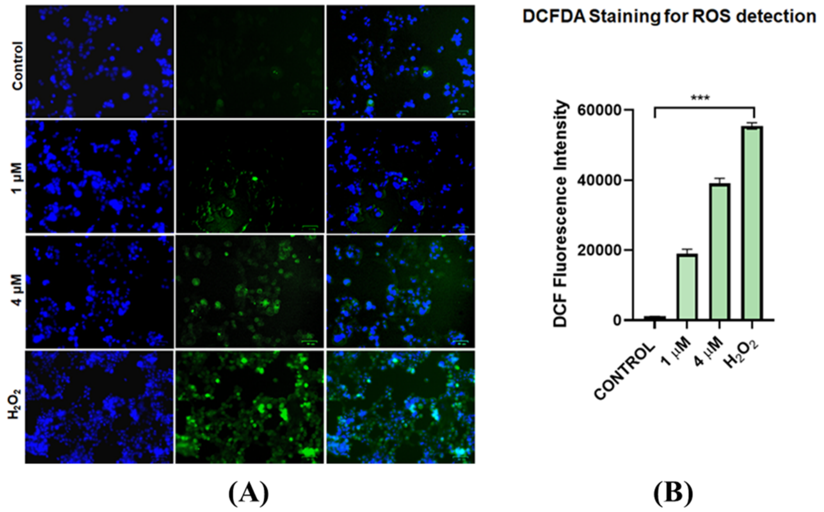

Figure 12. Measurement of ROS production in **IrL**-treated HCT-116 CD44+ CSCs: (A) ROS generation upon treatment with **IrL** doses 1 μM, 4 μM, and H_2O_2 (positive control) as obtained by DCFDA staining. Scale bar 50 μM. (B) Diagram indicating the average fluorescence intensity of DCF in **IrL**-treated, H_2O_2-treated, and untreated HCT-116 CD44+ CSCs. The resulting p value <0.0001 (***). The error bar represents the ± standard error of mean (SEM).

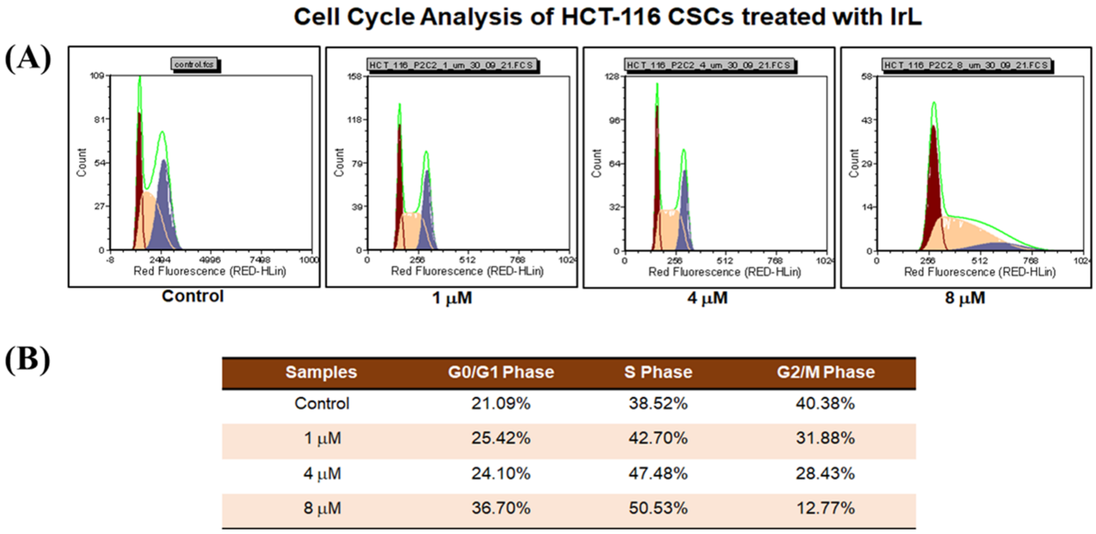

Samples	G0/G1 Phase	S Phase	G2/M Phase
Control	21.09%	38.52%	40.38%
1 μM	25.42%	42.70%	31.88%
4 μM	24.10%	47.48%	28.43%
8 μM	36.70%	50.53%	12.77%

Figure 13. Cell cycle analysis: (A) Cell cycle analysis of untreated and **IrL**-treated (1 μM, 4 μM, and 8 μM) HCT-116 CD44+CSCs. (B) Representative graphs of the cell cycle phases up on treatment with **IrL** complex. The p values <0.001 (**), and <0.0001(***) reflected statistical significance. Error bar signifies the ± standard error of mean (SEM).

other hand, the positive control cells treated with H_2O_2 exhibited relatively high ROS production (Figure 12).

***IrL* Complex Mediated a G0/G1 Cell Cycle Arrest at the Highest Tested Concentration of 8 μM.** To demonstrate the inhibitory effect of the **IrL** complex on the cell cycle of colorectal cancer stem cells, cell cycle analysis was carried out with synchronized HCT-116 CD44+ CSCs. The control CSCs without any treatment exhibited increased S- phase (38.52%) and G2/M phase (40.38%), followed by a G0/G1 phase with 21.09% cells (Figure 13A). On the contrary, **IrL** complex treatment of colorectal CSCs reduced G2/M phase cells by up to 12.77%, and the **IrL** complex induced a slight increase in S-phase cells by ∼12%. Interestingly, the **IrL** treatment significantly increased G0/G1 cells (36.70%), suggestive of a possible G1 arrest at the highest tested dose, i.e., 8 μM. Moreover, increased S-phase (50.53%) cells at the highest tested dose of 8 μM is possibly indicative of a drug-resistant proliferating population that requires further validation.

*Annexin V-FITC/PI Assay Revealed Significant Apoptotic Induction Mediated by **IrL** Complex on HCT-116 Colorectal CSCs.* To demonstrate the apoptotic induction mediated by **IrL** complex on HCT-116 CD44+ CSCs, Annexin V-FITC/PI assay has been performed. It is evident from Figure 14 that the complex, at a concentration of 4 μM, showed that around 18.96% of cells were discovered to be exhibiting apoptotic induction. These findings suggest the potential of the **IrL** complex for apoptotic induction in HCT-116 CD44+ CSCs.

***IrL*-Treated HCT-116 CSCs Demonstrated Increased Expression of Proapoptotic Factor BAX.** The treatment of HCT-116 CD44+ CSCs with IrL complex led to enhanced expression of the proapoptotic factor BAX, as shown by Annexin V-FITC/PI investigation. Interestingly, the antiapoptotic Bcl-2 displayed a significant upregulation relative to the control. The increased Bcl-2 expression can be correlated to the inhibition of autophagy, as autophagy is crucial for the maintenance of CSC populations. Cancer stem cells are known

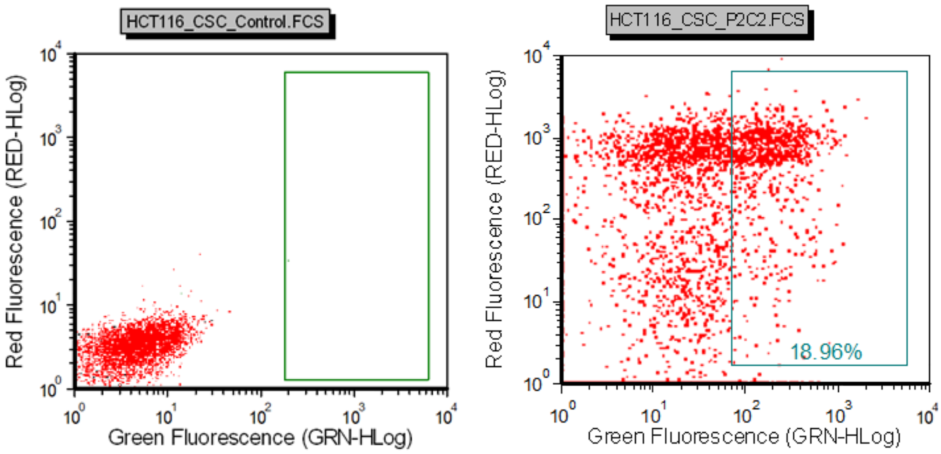

Figure 14. Apoptosis assay: Detection of apoptotic cells in HCT-116 CD44+ CSCs subjected with **IrL** with the help of Annexin V-FITC/PI assay. Nineteen percent of the cells underwent apoptosis when exposed to a compound concentration of 4 μM.

to exploit strategies like modulation of autophagy, high glycolytic flux, and redox signaling, to circumvent nutritional deficiency and avoid cell death.[46] The cross-talk between apoptosis and autophagy is regulated by interaction of Bcl-2 and beclin-1. Bcl-2 interacts with beclin-1 (via BH3 domain), resulting in the inhibition of preautophagosomal assembly by beclin-1, leading to the inhibition of autophagy.[47] Phosphorylation (Figure 15) of Bcl-2 aids in the displacement of Bcl-2 from beclin-1 and the induction of autophagy.[48]

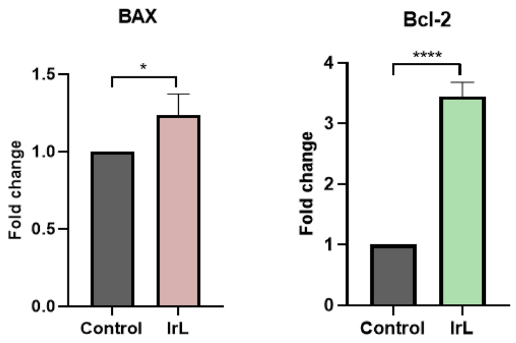

Figure 15. Detection of BAX/Bcl-2 expression in **IrL**-treated HCT-116 CSCs by qRT PCR.

*qRT PCR for Detecting the Involvement of Autophagy in **IrL**-Treated HCT-116 CSCs.* Furthermore, to confirm mitochondrial abnormalities, we performed a quantitative reverse transcription polymerase chain reaction (qRT PCR) to understand the involvement of autophagy mediated by the **IrL** complex in HCT-116 CSCs. The expression of potential autophagy markers LC3, PINK-1, and PRKN was analyzed in control and **IrL** treated cells with respect to GAPDH (Figure 16).

CONCLUSION

Our study successfully established the dose-dependent cytotoxic potential of **IrL** on HCT-116 colorectal cancer stem cells (CRCSCs). Further colocalization and immunochemistry study of the complex **IrL** revealed the subcellular localization of the compound in the nucleus and other parts of the cytoplasm and created nuclear DNA damage and mitochondrial dysfunction. A significant increase in mitochondrial dysfunction, initiated by alterations in MMP and subsequent ROS generation, was facilitated by complex **IrL**. Complex **IrL** was further explored to unravel the effect of the complex on cell cycle of colorectal CSCs. At the highest tested dose of 8 μM, we were able to clearly define the role of the IrL complex in causing a G0/G1 phase cell cycle arrest. The Annexin V-FITC/PI assay revealed the potential of the **IrL** complex to mediate the apoptotic pathway. The level of BAX and Bcl-2 was further quantified by qRT PCR. The expression of proapoptotic BAX showed increased expression in **IrL**-treated cells compared to the control, indicating the potential of **IrL** complex for apoptotic induction. In contrast, an increase in the antiapoptotic factor Bcl-2 was observed that may be

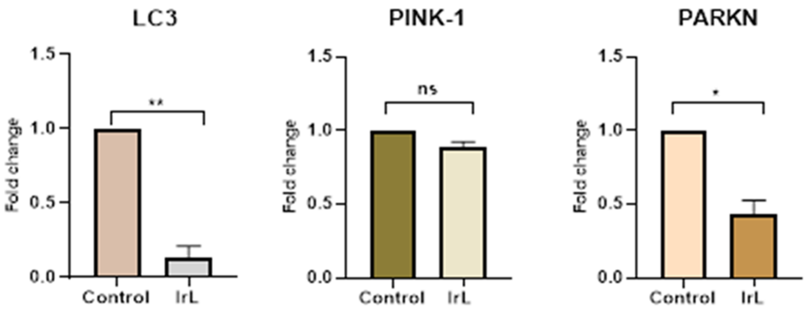

Figure 16. Detecting the expression of the autophagy genes by qRT-PCR: Bar graphs representing the expression of genes involved in autophagy process (LC3, PINK-1, and PARKN), followed by IrL treatment in HCT-116 CSCs. The observed p values were <0.001 (**), < 0.01 (*), and 0.053 (ns). The error bar denotes ± standard error of means (SEM).

linked with the inhibition of autophagy, the survival mechanism of CSCs by which the cells adapt to adverse microenvironmental conditions and meets the increased demand of nutrition. Moreover, the increase in the expression of antiapoptotic factor Bcl-2 can be correlated with the increase in the S-phase cells at the highest dose of treatment (8 μM), thereby indicating a possible increase in the drug-resistant population. Upon further validation, complex **IrL** was evolved as an inhibitor of autophagy for the eradication of cancer stem cells.

3. EXPERIMENTAL SECTION

Materials and Method. Throughout the entire experiment, only pure chemicals and solvents were used. 1,10-phenanthroline-5,6-dione, 4-bromo-*o*-phenylenediamine, dichloro-(pentamethylcyclopentadienyl)iridium(III)dimer, dichloro(*p*-cymene)ruthenium(II) dimer, pentacarbonylchlororhenium(I), ammonium hexafluorophosphate, naphthalene-1-boronic acid, potassium carbonate, tetrakis(triphenylphosphine)palladium(0), deoxyribonucleic acid sodium salt (DNA), bovine serum albumin (BSA), and L-glutathione reduced (GSH) were acquired from Sigma-Aldrich Chemical Limited, Spectrochem, and E-Merck. HCT-116 cells were obtained from the National Center for Cell Science (NCCS) in Pune. A powerful Bruker DPX spectrometer was utilized to record all the NMR spectra, with tetramethylsilane (TMS) being employed as an internal reference. The obtained chemical shift values were described in ppm units. Here is a representation of the various peaks that can be found: s, singlet; d, doublet; dd, double doublet; t, triplet; m, multiplet; brs, broad singlet. Elchem Microprocessor-based DT equipment was used to measure the melting points of the complexes. An Ostwald viscometer was used for the experiments on viscosity, and a TDS conductometer-307 was used to measure the conductivity of the complexes. Shimadzu Affinity FT-IR spectra were taken in the range of 4000−400 cm^{-1} and indicated strong (s), weak (w), medium (m), and very strong bands (vs) in the infrared (IR) spectra of the complexes. The mass spectra of the compounds were noted on employing the solvents acetonitrile and methanol. The JASCO V-730 spectrophotometer with a 1 cm quartz cell was used for the UV−visible experiment, while the Hitachi F7000 fluorescence spectrophotometer with a xenon lamp was used to obtain the fluorescence spectra. The cytotoxicity (MTT assay) was performed using an Elisa reader and a 96-well plate. PerkinElmer equipment was used for the elemental analysis.

Chemistry. *Synthetic Technique of **L′**.* First, a methanolic solution of 50 mg of 1,10-phenanthroline-5,6-dione (0.238 mmol, 1 equiv) was stirred at rt for 2 h after 49 mg of 4-bromo-o-phenylenediamine (0.262 mmol, 1 equiv) was added. Thin layer chromatography was used to detect the reaction. [silica gel; ethyl acetate: methanol (2:1)]. Once the reaction was complete, the methanol was evaporated, and the black solid was washed with hexane and diethyl ether. Thereafter, the solid was dried and prepared for the subsequent process.

Yield: 92%; Color: black; Mp: 148 °C; R_f [ethyl acetate: methanol (2:1)]: 0.61; IR (cm^{-1}): υ Ar C−H stretching (3143,), C = N stretching (1604, m), Ar C═C stretching (1460), Ar C−H bending (721), C−Br stretching (626); ^{1}H NMR (DMSO-d_6, 400 MHz): δ 9.49−9.46 (m, 2H, ArH), 9.23−9.21(m, 2H, ArH), 8.61 (d, 1H, *J* = 2.0 Hz, ArH), 8.32 (t, 1H, *J* = 8.8 Hz, ArH), 8.17−8.14 (m, 1H, ArH), 7.97−7.94 (m, 2H, ArH); ^{13}C NMR (DMSO-d_6, 100 MHz): δ 153.18, 153.07, 148.43, 145.98, 142.72, 142.03, 141.0, 137.73, 134.84, 133.65, 131.53, 127.27, 125.11, 119.56; ESI-MS (MeOH): *m*/*z* = 361.7 [M + H]$^+$.

*Synthetic Technique of **L**.* Naphthalene-1-boronic acid (50 mg, 0.291 mmol, 1 equiv), potassium carbonate (200 mg, 1.45 mmol, 5 equiv), and tetrakis(triphenylphosphine) palladium(0) (33 mg, 0.03 mmol, 0.1 equiv) were combined in isopropanol (10 mL) and stirred at rt. Reflux was maintained at 70 °C after 105 mg of compound **L′** (0.291 mmol, 1 equiv) was introduced after 20 min of stirring for 3 h. After the reaction was complete, we filtered the entire mixture and then evaporated the isopropanol from the filtrate to obtain the final result, a brownish solid. The solid was then purified by washing several times with hexane and diethyl ether.

Yield: 65%; Color: brown; Mp: 130 °C; R_f [ethyl acetate: methanol (2:1)]: 0.68; IR (cm^{-1}): υ Ar C−H stretching (3294, m), C═N stretching (1591, m), Ar C═C stretching (1420, m), Ar C−H bending (721, s); ^{1}H NMR (DMSO-d_6, 400 MHz): δ 9.55 (d, 2H, *J* = 8.0 Hz, ArH), 9.22 (t, 3H, *J* = 2.0 Hz, ArH), 8.41−8.38 (m, 2H, ArH), 8.07−8.05 (m, 2H, ArH), 7.96−7.93 (m, 3H, ArH), 7.64−7.59 (m, 2H, ArH), 7.57−7.55 (m, 2H, ArH); ^{13}C NMR (DMSO-d_6, 100 MHz): δ 153.06, 152.95, 148.41, 148.27, 142.42, 141.73, 141.41, 140.80, 134.71, 133.52, 133.46, 132.52, 132.49, 132.00, 131.90, 131.39, 129.29, 129.17, 128.54, 127.04, 126.94, 125.47, 124.96, 124.86; ESI-MS (MeOH): *m*/*z* = 409.23 [M + H]$^+$.

*Synthetic Technique of **RuL**.* According to the previous work,[49] 20 mg of ligand **L** (0.049 mmol, 1 equiv) and 14 mg of [Ru$_2^{II}$(η6-*p*-cym)$_2$(Cl)$_4$] (0.023 mmol, 0.5 equiv.) were used to synthesis **RuL**. At last, the brown colored complex formed.

Yield: 95%; Color: brown; Mp: 182 °C; R_f (pure methanol): 0.57; IR (cm^{-1}): υ Ar C−H stretching (3294, m), sp^3 C−H stretching (3053, m), C═N stretching (1591, m), Ar C═C stretching (1410, m), P−F stretching (831, s), Ar C−H bending (723, s); ^{1}H NMR (DMSO-d_6, 400 MHz): δ 10.10 (dd, 2H, *J* = 5.6 Hz, ArH), 9.74−9.61 (m, 3H, ArH), 8.67 (s, 1H, ArH), 8.53 (t, 1H, *J* = 8.8 Hz, ArH), 8.35−8.22 (m, 5H, ArH), 8.07 (d, 1H, *J* = 8.0 Hz, ArH), 7.89 (d, 1H, *J* = 8.0 Hz, ArH), 7.73−7.58 (m, 2H, ArH), 6.44 (d, 2H, *J* = 6.4 Hz, *p*-cymene ArH), 6.21 (d, 2H, *J* = 6.4 Hz, *p*-cymene ArH), 2.72−2.70 (m, 1H, *p*-cymene aliphatic −CH proton), 2.22 (s, 3H, *p*-cymene aliphatic methyl proton), 1.03 (d, 6H, *J* = 8.0 Hz, *p*-cymene isopropyl methyl proton); ^{13}C NMR (DMSO-d_6, 100 MHz): δ 158.11, 157.12, 150.20, 148.57, 146.86, 142.91, 141.33, 140.56, 135.91, 132.53, 132.0, 131.90, 129.75, 129.30, 129.18, 128.21, 116.11, 119.4, 106.87 (*p*-cymene ArC), 100.57 (*p*-cymene ArC), 86.83 (*p*-cymene ArCH), 86.43 (*p*-cymene ArCH), 85.98 (*p*-cymene ArCH), 84.68 (*p*-cymene ArCH), 30.92 (isopropyl −CH), 22.24 (isopropyl − CH$_3$), 21.96 (isopropyl − CH$_3$); 18.73 (*p*-cymene −CH$_3$); ^{19}F NMR (DMSO-d_6, 376 MHz): δ −71.04 (PF$_6$), −69.16 (PF$_6$); ^{31}P NMR (DMSO-d_6, 162 MHz): δ −153.02 to −135.46 (PF$_6$); HRMS (MeOH): *m*/*z* = 679.1202 (calculated), 679.1212 (observed) [M-PF$_6$]$^+$. Anal. Calcd for $C_{38}H_{30}N_4ClF_6PRu$: C, 55.38; H, 3.67; N, 6.80. Found: C, 54.89; H, 3.62; N, 6.88.

*Synthetic Technique of **IrL**.* According to the previous work,[50] 20 mg of ligand **L** (0.049 mmol, 1 equiv.) and 19 mg of [Ir$_2^{III}$(η^5-*cp**)$_2$(Cl)$_4$] (0.024 mmol, 0.5 equiv.) were used to synthesis **RuL**. At last, lemon-yellow colored complex formed.

Yield: 94%; Color: Lemon Yellow; Mp: 188 °C; R_f (pure methanol): 0.52; IR (cm^{-1}): υ Ar C−H stretching (3319, m), sp^3 C−H stretching (2980, m), C = N stretching (1626, m), Ar C = C stretching (1431, m), P−F stretching (827, s), Ar C−H bending (760, s); ^{1}H NMR (DMSO-d_6, 400 MHz): δ 9.79−9.66 (m, 3H, ArH), 9.51 (t, 2H, *J* = 6.8 Hz, ArH), 8.70 (s, 1H, *J* = ArH), 8.56 (t, 1H, *J* = 8.8 Hz, ArH), 8.42−8.35 (m, 4H, ArH), 8.27 (t, 1H, *J* = 7.6 Hz, ArH), 8.05 (d, 1H, *J* = 8.0 Hz, ArH), 7.89 (d, 1H, *J* = 8.0 Hz, ArH), 7.73−7.58 (m, 2H, ArH), 1.75 (s, 15H, H-a −H-e, Cp* protons); ^{13}C NMR (DMSO-d_6, 100 MHz): δ 154.32, 151.24, 149.89, 147.19, 145.85, 144.79, 140.84, 136.41, 133.80, 132.53, 132.0, 131.90, 129.30, 129.18, 128.12, 121.38, 116.11, 92.57 (Cp* ring carbons), 89.89 (Cp* ring carbons), 8.71 (Cp* CH$_3$ carbons); ^{19}F NMR (DMSO-d_6, 376 MHz): δ −71.04 (PF$_6$), −69.16 (PF$_6$); ^{31}P NMR (DMSO-d_6, 162 MHz): δ −153.02 to −135.46 (PF$_6$); HRMS (MeOH): *m*/*z* = 771.1866 (calculated), 771.1861 (observed) [M-PF$_6$]$^+$. Anal. Calcd for $C_{38}H_{31}N_4ClF_6PIr$: C, 49.81; H, 3.41; N, 6.11. Found: C, 49.66; H, 3.40; N, 6.02.

*Synthetic Technique of **ReL**.* One equivalent of [(CO)$_5$Re^{I}Cl] (30 mg, 0.083 mmol) was combined with 1 equiv. of compound **L** (34 mg, 0.082 mmol) in 5 mL of acetonitrile and refluxed for 6 h at 70 °C to synthesize **ReL**. As soon as the reaction was complete, the solid was extracted by evaporating the solvent, washed with hexane and diethyl ether, and then dried in air.

Yield: 92%; Color: yellow; Mp: 162 °C; R_f (pure methanol): 0.73; IR (cm^{-1}): υ Ar C−H stretching (3327, m), C = O stretching (2017, vs; 1882, vs), C=N stretching (1641, m), Ar C=C stretching (1410, m), Ar C−H bending (725, s); ^{1}H NMR (DMSO-d_6, 400 MHz): δ 9.73 (t, 3H, J = 8.4 Hz, ArH), 9.56 (dd, 2H, J = 6.0 Hz, ArH), 8.64 (s, 1H, ArH), 8.51 (t, 1H, J = 8.4 Hz, ArH), 8.32−8.21 (m, 5H, ArH), 8.06 (d, 1H, J = 8.0 Hz, ArH), 7.90 (d, 1H, J = 3.2 Hz, ArH), 7.71−7.55 (m, 2H, ArH); ^{13}C NMR (DMSO-d_6, 100 MHz): δ 190.12 (carbonyl carbons), 182.50 (carbonyl carbons), 172.07 (carbonyl carbons), 155.55, 150.26, 149.62, 142.82, 141.26, 140.30, 136.41, 136.02, 132.66, 132.53, 132.0, 131.90, 131.76, 130.36, 130.20, 129.29, 129.18, 128.52, 126.35, 125.47, 116.11; ^{19}F NMR (DMSO-d_6, 376 MHz): δ −71.06 (PF_6), −69.17 (PF_6); ^{31}P NMR (DMSO-d_6, 162 MHz): δ −157.38 to −131.03 (PF_6); HRMS (MeOH): m/z = 720.1045 (calculated), 720.1027 (observed) [M-Cl+CH_3CN]$^+$. Anal. Calcd for $C_{31}H_{16}N_4O_3ClRe$: C, 52.14; H, 2.26; N, 7.85. Found: C, 52.49; H, 2.31; N, 7.79.

■ ASSOCIATED CONTENT

Supporting Information

The Supporting Information is available free of charge at https://pubs.acs.org/doi/10.1021/acsabm.2c00556.

> UV, liquid chromatography−mass spectrometry (LCMS), high resolution mass spectrometry (HRMS), fluorescence spectra, NMR, infrared (IR), and other spectral information for all compounds mentioned in this article (PDF)

■ AUTHOR INFORMATION

Corresponding Authors

Priyankar Paira − *Department of Chemistry, School of Advanced Sciences, Vellore Institute of Technology, Vellore 632014 Tamilnadu, India;* orcid.org/0000-0003-1698-4895; Email: priyankar.paira@vit.ac.in

Bipasha Bose − *Department Stem Cells and Regenerative Medicine Centre, Institution Yenepoya Research Centre, Yenepoya University, Mangalore 575018 Karnataka, India;* Email: bipasha.bose@gmail.com

Authors

Utpal Das − *Department of Chemistry, School of Advanced Sciences, Vellore Institute of Technology, Vellore 632014 Tamilnadu, India*

Shanooja Shanavas − *Department Stem Cells and Regenerative Medicine Centre, Institution Yenepoya Research Centre, Yenepoya University, Mangalore 575018 Karnataka, India*

Apoorva H. Nagendra − *Department Stem Cells and Regenerative Medicine Centre, Institution Yenepoya Research Centre, Yenepoya University, Mangalore 575018 Karnataka, India*

Binoy Kar − *Department of Chemistry, School of Advanced Sciences, Vellore Institute of Technology, Vellore 632014 Tamilnadu, India;* orcid.org/0000-0002-2059-6900

Nilmadhab Roy − *Department of Chemistry, School of Advanced Sciences, Vellore Institute of Technology, Vellore 632014 Tamilnadu, India*

Seshu Vardhan − *Department of Applied Chemistry, S. V. National Institute of Technology (SVNIT) Ichchanath, Surat 395007 Gujrat, India;* orcid.org/0000-0002-8906-5243

Suban K Sahoo − *Department of Applied Chemistry, S. V. National Institute of Technology (SVNIT) Ichchanath, Surat 395007 Gujrat, India;* orcid.org/0000-0003-1751-5310

Debashis Panda − *Department of Chemistry, Rajiv Gandhi Institute of Petroleum Technology (Institute of National Importance (GOI Act. 54/2007), Jais 229304 Uttar Pradesh, India;* orcid.org/0000-0002-2333-3735

Complete contact information is available at: https://pubs.acs.org/10.1021/acsabm.2c00556

Author Contributions

†U.D. and S.S. contributed equally.

Notes

The authors declare no competing financial interest.

■ ACKNOWLEDGMENTS

The authors are grateful to the Department of Science and Technology, Government of India, for supporting their work through the DST-SERB CRG project grant (CRG/2021/002267). The authors are grateful to Vellore Institute of Technology for providing VIT SEED funding. We acknowledge DST, New Delhi, India, for DST-FIST project.

■ REFERENCES

(1) *Global Facts and Figures 2007 Rev2P*; American Cancer Society: Atlanta, 2007.

(2) Thun, M. J.; DeLancey, J. O.; Center, M. M.; Jemal, A.; Ward, E. M. The Global Burden of Cancer: Priorities for Prevention. *Carcinogenesis* **2010**, *31* (1), 100−110.

(3) Kauffman, S. Homeostasis and differentiation in random genetic control networks. *Nature* **1969**, *224*, 177−178.

(4) Ndagi, U.; Mhlongo, N.; Soliman, M. E. Metal Complexes in Cancer Therapy − An Update from Drug Design Perspective. *Drug Des. Devel. Ther.* **2017**, *11*, 599−616.

(5) Naik, A.; Rubbiani, R.; Gasser, G.; Spingler, B. Visible-Light-Induced Annihilation of Tumor Cells with Platinum-Porphyrin Conjugates. *Angew. Chem.* **2014**, *126* (27), 7058−7061.

(6) Zou, T.; Liu, J.; Lum, C. T.; Ma, C.; Chan, R. C. -T.; Lok, C.-N.; Kwok, W.-M.; Che, C.-M. Luminescent Cyclometalated Platinum (II) Complex Forms Emissive Intercalating Adducts with Double-Stranded DNA and RNA: Differential Emissions and Anticancer Activities. *Angew. Chem.* **2014**, *126* (38), 10283−10287.

(7) Zhang, J. J.; Lu, W.; Sun, R. W. Y.; Che, C. M. Organogold (III) Supramolecular Polymers for Anticancer Treatment. *Angew. Chemie - Int. Ed.* **2012**, *51* (20), 4882−4886.

(8) Li, Z.; David, A.; Albani, B. A.; Pellois, J. P.; Turro, C.; Dunbar, K. R. Optimizing the Electronic Properties of Photoactive Anticancer Oxypyridine-Bridged Dirhodium (II, II) Complexes. *J. Am. Chem. Soc.* **2014**, *136* (49), 17058−17070.

(9) Kar, B.; Roy, N.; Pete, S.; Moharana, P.; Paira, P. Ruthenium and iridium based mononuclear and multinuclear complexes: A Breakthrough of Next-Generation anticancer metallopharmaceuticals. *Inorg. Chim. Acta* **2020**, *512*, 119858.

(10) Chelopo, M. P.; Pawar, S. A.; Sokhela, M. K.; Govender, T.; Kruger, H. G.; Maguire, G. E. M. Anticancer Activity of Ruthenium (II) Arene Complexes Bearing 1,2,3,4-Tetrahydroisoquinoline Amino Alcohol Ligands. *Eur. J. Med. Chem.* **2013**, *66*, 407−414.

(11) Frik, M.; Martínez, A.; Elie, B. T.; Gonzalo, O.; Ramírez de Mingo, D.; Sanaú, M.; Sánchez-Delgado, R.; Sadhukha, T.; Prabha, S.; Ramos, J. W.; Marzo, I.; Contel, M. In Vitro and in Vivo Evaluation of Water-Soluble Iminophosphorane Ruthenium (II) Compounds. A Potential Chemotherapeutic Agent for Triple Negative Breast Cancer. *J. Med. Chem.* **2014**, *57* (23), 9995−10012.

(12) Seršen, S.; Kljun, J.; Kryeziu, K.; Panchuk, R.; Alte, B.; Körner, W.; Heffeter, P.; Berger, W.; Turel, I. Structure-Related Mode-of-Action Differences of Anticancer Organoruthenium Complexes with β-Diketonates. *J. Med. Chem.* **2015**, *58* (9), 3984−3996.

(13) Xie, Y.; Zhang, S.; Ge, X.; Ma, W.; He, X.; Zhao, Y.; Ye, J.; Zhang, H.; Wang, A.; Liu, Z. Lysosomal-Targeted Anticancer Half-

Sandwich Iridium (III) Complexes Modified with Lonidamine Amide Derivatives. *Appl. Organomet. Chem.* **2020**, *34* (5), 1−13.

(14) He, X.; Tian, M.; Liu, X.; Tang, Y.; Shao, C. F.; Gong, P.; Liu, J.; Zhang, S.; Guo, L.; Liu, Z. Triphenylamine-Appended Half-Sandwich Iridium (III) Complexes and Their Biological Applications. *Chem. - An Asian J.* **2018**, *13* (11), 1500−1509.

(15) Du, Q.; Guo, L.; Tian, M.; Ge, X.; Yang, Y.; Jian, X.; Xu, Z.; Tian, Z.; Liu, Z. Potent Half-Sandwich Iridium (III) and Ruthenium (II) Anticancer Complexes Containing a P∧O-Chelated Ligand. *Organometallics* **2018**, *37* (17), 2880−2889.

(16) Liu, Z.; Romero-Canelón, I.; Habtemariam, A.; Clarkson, G. J.; Sadler, P. J. Potent Half-Sandwich Iridium (III) Anticancer Complexes Containing C∧N-Chelated and Pyridine Ligands. *Organometallics* **2014**, *33* (19), 5324−5333.

(17) Capper, M. S.; Packman, H.; Rehkämper, M. Rhenium-Based Complexes and in Vivo Testing: A Brief History. *ChemBioChem.* **2020**, *21* (15), 2111−2115.

(18) He, L.; Pan, Z. Y.; Qin, W. W.; Li, Y.; Tan, C. P.; Mao, Z. W. Impairment of the Autophagy-Related Lysosomal Degradation Pathway by an Anticancer Rhenium(i) Complex. *Dalt. Trans.* **2019**, *48* (13), 4398−4404.

(19) Ye, R. R.; Tan, C. P.; Chen, M. H.; Hao, L.; Ji, L. N.; Mao, Z. W. Mono- and Dinuclear Phosphorescent Rhenium(I) Complexes: Impact of Subcellular Localization on Anticancer Mechanisms. *Chem. - A Eur. J.* **2016**, *22* (23), 7800−7809.

(20) Darshani, T.; Fronczek, F. R.; Priyadarshani, V. V.; Samarakoon, S. R.; Perera, I. C.; Perera, T. Synthesis and Characterization of Novel Naphthalene-Derivatized Tridentate Ligands and Their Net Neutral Rhenium Tricarbonyl Complexes and Cytotoxic Effects on Non-Small Cell Lung Cancer Cells of Interest. *Polyhedron* **2020**, *187*, 114652.

(21) Mondal, A.; Paira, P. Hypoxia Efficient and Glutathione-Resistant Cytoselective Ruthenium (II)-p-Cymene-Arylimidazophenanthroline Complexes: Biomolecular Interaction and Live Cell Imaging. *Dalt. Trans.* **2020**, *49* (36), 12865−12878.

(22) He, L.; Li, Y.; Tan, C. P.; Ye, R. R.; Chen, M. H.; Cao, J. J.; Ji, L. N.; Mao, Z. W. Cyclometalated Iridium (III) Complexes as Lysosome-Targeted Photodynamic Anticancer and Real-Time Tracking Agents. *Chem. Sci.* **2015**, *6* (10), 5409−5418.

(23) Steunenberg, P.; Ruggi, A.; Van Den Berg, N. S.; Buckle, T.; Kuil, J.; Van Leeuwen, F. W. B.; Velders, A. H. Phosphorescence Imaging of Living Cells with Amino Acid-Functionalized Tris(2-Phenylpyridine) Iridium (III) Complexes. *Inorg. Chem.* **2012**, *51* (4), 2105−2114.

(24) Das, U.; Kar, B.; Pete, S.; Paira, P. Ru (II), Ir(III), Re(I) and Rh(III) Based Complexes as next Generation Anticancer Metallopharmaceuticals. *Dalt. Trans.* **2021**, *50* (32), 11259−11290.

(25) Leonidova, A.; Gasser, G. Underestimated Potential of Organometallic Rhenium Complexes as Anticancer Agents. *ACS Chem. Biol.* **2014**, *9* (10), 2180−2193.

(26) Balasingham, R. G.; Coogan, M. P.; Thorp-Greenwood, F. L. Complexes in Context: Attempting to Control the Cellular Uptake and Localisation of Rhenium Fac-Tricarbonyl Polypyridyl Complexes. *Dalt. Trans.* **2011**, *40* (44), 11663−11674.

(27) Lo, K. K. W.; Louie, M. W.; Sze, K. S.; Lau, J. S. Y. Rhenium(I) Polypyridine Biotin Isothiocyanate Complexes as the First Luminescent Biotinylation Reagents: Synthesis, Photophysical Properties, Biological Labeling, Cytotoxicity, and Imaging Studies. *Inorg. Chem.* **2008**, *47* (2), 602−611.

(28) Holmlin, R. E.; Stemp, E. D. A.; Barton, J. K. Ru (Phen)$_2$dppz^{2+} Luminescence: Dependence on DNA Sequences and Groove-Binding Agents. *Inorg. Chem.* **1998**, *37* (1), 29−34.

(29) Roy, N.; Sen, U.; Ray Chaudhuri, S.; Muthukumar, V.; Moharana, P.; Paira, P.; Bose, B.; Gauthaman, A.; Moorthy, A. *Dalton Trans.* **2021**, *50*, 2268−2283.

(30) Rangasamy, S.; Ju, H.; Um, S.; Oh, D.-C.; Song, J. M. Mitochondria and DNA Targeting of 5,10,15,20-Tetrakis(7-sulfonatobenzo[b]thiophene) Porphyrin-Induced Photodynamic Therapy via Intrinsic and Extrinsic Apoptotic Cell Death. *J. Med. Chem.* **2015**, *58*, 6864−6874.

(31) Chen, Y.; Qiao, L.; Ji, L.; Chao, H. Phosphorescent Iridium (III) Complexes as Multicolor Probes for Specific Mitochondrial Imaging and Tracking. *Biomaterials* **2014**, *35* (1), 2−13.

(32) Jin, C.; Liu, J.; Chen, Y.; Zeng, L.; Guan, R.; Ouyang, C.; Ji, L.; Chao, H. Cyclometalated Iridium (III) Complexes as Two-Photon Phosphorescent Probes for Specific Mitochondrial Dynamics Tracking in Living Cells. *Chem. − A Eur. J.* **2015**, *21* (34), 12000−12010.

(33) Kubanik, M.; Holtkamp, H.; Söhnel, T.; Jamieson, S. M. F.; Hartinger, C. G. Impact of the Halogen Substitution Pattern on the Biological Activity of Organoruthenium 8-Hydroxyquinoline Anticancer Agents. *Organometallics* **2015**, *34* (23), 5658−5668.

(34) Gilewska, A.; Barszcz, B.; Masternak, J.; Kazimierczuk, K.; Sitkowski, J.; Wietrzyk, J.; Turlej, E. Similarities and Differences in D6 Low-Spin Ruthenium, Rhodium and Iridium Half-Sandwich Complexes: Synthesis, Structure, Cytotoxicity and Interaction with Biological Targets. *JBIC J. Biol. Inorg. Chem.* **2019**, *24* (4), 591−606.

(35) Aman, F.; Hanif, M.; Siddiqui, W. A.; Ashraf, A.; Filak, L. K.; Reynisson, J.; Söhnel, T.; Jamieson, S. M. F.; Hartinger, C. G. Anticancer Ruthenium(H6-p-Cymene) Complexes of Nonsteroidal Anti-Inflammatory Drug Derivatives. *Organometallics* **2014**, *33* (19), 5546−5553.

(36) (a) Geary, W. J. The Use of Conductivity Measurements in Organic Solvents for the Characterisation of Coordination Compounds. *Coord. Chem. Rev.* **1971**, 7 (1), 81−122. (b) Ali, I.; Wani, W. A.; Saleem, K. Empirical Formulae to Molecular Structures of Metal Complexes by Molar Conductance. *Synth. React. Inorganic, Met. Nano-Metal Chem.* **2013**, *43* (9), 1162−1170. (c) Banerjee, S.; Pant, I.; Khan, I.; Prasad, P.; Hussain, A.; Kondaiah, P.; Chakravarty, A. R. Remarkable Enhancement in Photocytotoxicity and Hydrolytic Stability of Curcumin on Binding to an Oxovanadium (IV) Moiety. *Dalt. Trans.* **2015**, *44* (9), 4108−4122.

(37) Saravanan, N.; Gandhi, M.; Senthil Kumar, A. High-Valent Ruthenium (IV)-Oxo Complex Stabilized Mesoporous Carbon (Graphitized)/Nafion Modified Electrocatalyst for Methanol Oxidation Reaction in Neutral PH. *J. Electroanal. Chem.* **2020**, *874*, 114457.

(38) Frisch, M. J.; Trucks, G. W.; Schlegel, H. B.; Scuseria, G. E.; Robb, M. A.; Cheeseman, J. R.; Montgomery, J. A., Jr.; Vreven, T.; Kudin, K. N.; Burant, J. C.; Millam, J. M.; Iyengar, S. S.; Tomasi, J.; Barone, V.; Mennucci, B.; Cossi, M.; Scalmani, G.; Rega, N.; Petersson, G. A.; Nakatsuji, H.; Hada, M.; Ehara, M.; Toyota, K.; Fukuda, R.; Hasegawa, J.; Ishida, M.; Nakajima, T.; Honda, Y.; Kitao, O.; Nakai, H.; Klene, M.; Li, X.; Knox, J. E.; Hratchian, H. P.; Cross, J. B.; Bakken, V.; Adamo, C.; Jaramillo, J.; Gomperts, R.; Stratmann, R. E.; Yazyev, O.; Austin, A. J.; Cammi, R.; Pomelli, C.; Ochterski, J. W.; Ayala, P. Y.; Morokuma, K.; Voth, G. A.; Salvador, P.; Dannenberg, J. J.; Zakrzewski, V. G.; Dapprich, S.; Daniels, A. D.; Strain, M. C.; Farkas, O.; Malick, D. K.; Rabuck, A. D.; Raghavachari, K.; Foresman, J. B.; Ortiz, J. V.; Cui, Q.; Baboul, A. G.; Clifford, S.; Cioslowski, J.; Stefanov, B. B.; Liu, G.; Liashenko, A.; Piskorz, P.; Komaromi, I.; Martin, R. L.; Fox, D. J.; Keith, T.; Al-Laham, M. A.; Peng, C. Y.; Nanayakkara, A.; Challacombe, M.; Gill, P. M. W.; Johnson, B.; Chen, W.; Wong, M. W.; Gonzalez, C.; Pople, J. A. *Gaussian C2*; Gaussian Inc.: Wallingford, CT, 2004.

(39) Morris, G. M.; Huey, R.; Lindstrom, W.; Sanner, M. F.; Belew, R. K.; Goodsell, D. S.; Olson, A. J. AutoDock4 and AutoDockTools4: Automated Docking with Selective Receptor Flexibility. *J. Comput. Chem.* **2009**, *30* (16), 2785−2791.

(40) Patra, S.; Santhosh, K.; Pabbathi, A.; Samanta, A. Diffusion of Organic Dyes in Bovine Serum Albumin Solution Studied by Fluorescence Correlation Spectroscopy. *RSC Adv.* **2012**, *2* (14), 6079−6086.

(41) (a) Liu, Z.-C.; Wang, B.-D.; Yang, Z.-Y.; Li, Y.; Qin, D.-D.; Li, T.-R. Synthesis, Crystal Structure, DNA Interaction and Antioxidant Activities of Two Novel Water-Soluble Cu (2+) Complexes Derivated from 2-Oxo-Quinoline-3-Carbaldehyde Schiff-Bases. *Eur. J. Med. Chem.* **2009**, *44* (11), 4477−4484. (b) Herebian, D.; Sheldrick, W.

S. Synthesis and DNA Binding Properties of Bioorganometallic (H5-Pentamethylcyclopentadienyl) Iridium (III) Complexes of the Type [(H5-C5Me5)Ir(Aa)(Dppz)]+ (Dppz = Dipyrido[3,2-a:2′,3′-c]-Phenazine, n = 1−3), with S-Coordinated Amino Acids (Aa) or Peptides. *J. Chem. Soc. Dalt. Trans.* **2002**, No. 6, 966−974. (c) Goll, J. G.; Holden Thorp, H. Oxidation of DNA by Trans-Dioxoruthenium (VI) Complexes: Self-Inhibition of DNA Cleavage by Metal Complexes. *Inorg. Chim. Acta* **1996**, *242* (1), 219−223. (d) Sarkar, B.; Mondal, A.; Madaan, Y.; Roy, N.; Moorthy, A.; Kuo, Y.-C.; Paira, P. Luminescent Anticancer Ruthenium (II)-p-Cymene Complexes of Extended Imidazophenanthroline Ligands: Synthesis, Structure, Reactivity, Biomolecular Interactions and Live Cell Imaging. *Dalt. Trans.* **2019**, *48* (32), 12257−12271. (e) Anuja, P. K.; Paira, P. Luminescent Anticancer Ru (II)-Arenebipyridine and Phenanthroline Complexes: Synthesis, Characterization, DFT Studies, Biological Interactions and Cellular Imaging Application. *J. Inorg. Biochem* **2020**, *208*, 111099. (f) Mondal, A.; Paira, P. Hypoxia Efficient and Glutathione-Resistant Cytoselective Ruthenium (II)-p-Cymene-Arylimidazophenanthroline Complexes: Biomolecular Interaction and Live Cell Imaging. *Dalt. Trans.* **2020**, *49* (36), 12865−12878. (g) Khan, T. A.; Bhar, K.; Thirumoorthi, R.; Roy, T. K.; Sharma, A. K. Design, Synthesis, Characterization and Evaluation of the Anticancer Activity of Water-Soluble Half-Sandwich Ruthenium (II) Arene Halido Complexes. *New J. Chem.* **2020**, *44* (1), 239−257. (h) Manikandan, R.; Chitrapriya, N.; Jang, Y. J.; Viswanathamurthi, P. Evaluation of DNA-Binding, Radical Scavenging and Cytotoxic Activity of Five Coordinated Cd (II) Complexes Containing 2-Acetylpyridine-N4-Substituted Thiosemicarbazone. *RSC Adv.* **2013**, *3* (29), 11647−11657.

(42) Roy, N.; Sen, U.; Madaan, Y.; Muthukumar, V.; Varddhan, S.; Sahoo, S. K.; Panda, D.; Bose, B.; Paira, P. Mitochondria-Targeting Click-Derived Pyridinyltriazolylmethylquinoxaline-Based Y-Shaped Binuclear Luminescent Ruthenium (II) and Iridium (III) Complexes as Cancer Theranostic Agents. *Inorg. Chem.* **2020**, *59* (23), 17689−17711.

(43) Shanavas, S.; Sen, U.; Sudheer Shenoy, P.; Bose, B. Redressal of the Molecular Mechanisms of Colon and Other Cancer Stem Cell Energetics/Oxidative Stress for Possible Translation. *Handbook of Oxidative Stress in Cancer: Therapeutic Aspects* **2022**, 978−981.

(44) Sen, U.; Chaudhury, D.; Shenoy P, S.; Bose, B. Differential Sensitivities of Triple-Negative Breast Cancer Stem Cell towards Various Doses of Vitamin C: An Insight into the Internal Antioxidant Systems. *J. Cell. Biochem.* **2021**, *122* (3−4), 349−366.

(45) Bose, B.; Kapoor, S.; Sen, U.; Nihad AS, M.; Chaudhury, D.; Shenoy P, S. Assessment of Oxidative Damage in the Primary Mouse Ocular Surface Cells/Stem Cells in Response to Ultraviolet-C (UV-C) Damage. *JoVE* **2020**, No. 156, e59924.

(46) Ojha, R.; Bhattacharyya, S.; Singh, S. K. Autophagy in Cancer Stem Cells: A Potential Link Between Chemoresistance, Recurrence, and Metastasis. *Biores. Open Access* **2015**, *4* (1), 97−108.

(47) Liang, X. H.; Kleeman, L. K.; Jiang, H. H.; Gordon, G.; Goldman, J. E.; Berry, G.; Herman, B.; Levine, B. Protection against Fatal Sindbis Virus Encephalitis by Beclin, a Novel Bcl-2-Interacting Protein. *J. Virol.* **1998**, *72* (11), 8586−8596.

(48) Minciullo, P. L.; Navarra, M.; Calapai, G.; Gangemi, S. Cytokine Network Involvement in Subjects Exposed to Benzene. *J. Immunol. Res.* **2014**, *2014*, 937987.

(49) Kar, B.; Das, U.; De, S.; Pete, S.; Sharma S, A.; Roy, N.; SK, A. K.; Panda, D.; Paira, P. GSH-Resistant and Highly Cytoselective Ruthenium(II)-p-Cymene-(Imidazo[4,5-f][1,10]Phenanthrolin-2-Yl)-Phenol Complexes as Potential Anticancer Agents. *Dalt. Trans.* **2021**, *50* (30), 10369−10373.

(50) Kar, B.; Shanavas, S.; Nagendra, A. H.; Das, U.; Roy, N.; Pete, S.; Sharma S, A.; De, S.; Kumar S K, A.; Vardhan, S.; Sahoo, S. K.; Panda, D.; Shenoy, S.; Bose, B.; Paira, P. Iridium(III)−Cp*-(Imidazo[4,5-f][1,10]Phenanthrolin-2-Yl)Phenol Analogues as Hypoxia Active, GSH-Resistant Cancer Cytoselective and Mitochondria-Targeting Cancer Stem Cell Therapeutic Agents. *Dalt. Trans.* **2022**, *51* (14), 5494−5514.